ISBN 91-628-3187-9

LUNFD6/(NFFL-7160)1998

Luminosity Measurement for the 1995 Z^0 scan with the Very Small Angle Tagger of DELPHI

September 10, 1998

Thesis Submitted for the Degree of
Filosofie Licentiat
by

Christina Jarlskog
Physics Department
Lund University
Sweden

To my parents,
Varvara and Petros

Contents

Abstract

This report presents analysis of LEP1 data from the Very Small Angle Tagger (VSAT) of the DELPHI detector at LEP. The VSAT is an electromagnetic sampling calorimeter consisting of four modules placed symmetrically at 7.7 m from the DELPHI origin. The process under study is Bhabha scattering at small polar angles (5-7 mrad). We discuss the beam parameter analysis for the 1995 Z^0 scan data. The detector simulation procedure is described in connection with the relative luminosity determination for the same period. The application of this measurement to the extraction of the hadronic lineshape parameters of the Z^0 particle is also presented.

Preface

In this report, we describe the analysis of data from the DELPHI VSAT detector at Z^0 energies with the purpose to obtain beam parameter information and the relative luminosity measurement that is used for the lineshape studies. The organisation of the report is as follows:

Chapter 1 contains a general description of the LEP ring and the components of the DELPHI detector with emphasis put on the VSAT detector.

Chapter 2 gives a short discussion on obtaining online and offline luminosity while chapter 3 discusses the theoretical fundamentals of the process used for the latter measurement, i.e. the Bhabha scattering.

Chapter 4 describes the offline procedure for collecting Bhabha events. Energy measurement, background subtraction, acceptance cuts and removal of corrupted events for 1995 scan data are discussed in detail.

Chapter 5 deals with the determination of beam parameters such as beamspot and acollinearity through the dependence of the detector's measures on those parameters.

Chapter 6 describes the detector simulation and the correction of the cross section due to beam parameter variations in terms of quantities directly measured by the detector.

Finally, in chapter 7, we combine the Bhabha sample obtained in chapter 4 with the cross section corrections derived in chapter 6 to calculate the integrated relative luminosity for the 1995 scan data taking. This result is then used for the DELPHI precision measurement of the Z^0 resonance parameters, which is described in Appendix A.

Chapter 1

LEP and DELPHI

1.1 The Large Electron-Positron storage ring

LEP started to operate in August 1989 and it is the largest accelerator yet built. It accelerates electrons and positrons in opposite directions in a vacuum pipe inside a retaining ring of magnets, before inducing them to collide head-on. Four detectors have been constructed to study the products of these collisions: ALEPH, L3, OPAL and DELPHI.

1.1.1 The beginning of LEP

The early development of the LEP ring can be highlighted by the following extracts of Sir John Adams' Annual Reports to the CERN Council in 1979 and 1980 [1]:

'Studies of the design of the LEP machines started at CERN in 1976 and the first practical design was published in 1978. This machine had a cost-optimized energy of 70 GeV per beam and measured 22 km in circumference. After extensive discussions during the autumn of 1978 it was decided to embark on the design of a somewhat larger machine, 30 km in circumference, with a cost-optimized energy of about 90 GeV per beam. The energy of both these machines could be extended, by using superconducting RF cavities, when these become available, to 100 and 130 GeV respectively.'

'Studies of the 30 km machine were completed during 1979 and a design report was issued in August.... The basic feature of the present LEP design is a large machine circumference in which the machine will be installed in stages corresponding to the new physics events that are predicted by the unified theory of weak and electromagnetic interactions. The first predicted event is the ... Z^0 at an energy of 90 GeV. Since these bosons can be produced singly, the LEP machine energy is about 50 GeV per beam, giving 100 GeV in the centre of mass. The next predicted event is the production of pairs of the charged intermediate bosons (W^+W^-) at an energy of about 180 GeV which requires LEP energies of about 90 GeV per beam.... The latest development of the LEP Project is to use the PS and SPS machines as the injectors for LEP.'

1.1.2 The tunnel

The most impressive part of the collider is the 26.67 km Main Ring tunnel. The remainder of the underground structure consists of the four experimental caverns, 18 pits, 3 km of secondary tunnel, and some 60 chambers and alcoves. The plane of the tunnel has been inclined by 1.4 % so that all underground caverns and the main part of the tunnel would be located in solid rock.

The guidance of the tunnelling machines on their desired trajectory was performed with a precision of about 1 cm and the alignment of the collider components within the LEP tunnel was done to a short-range relative precision of less than about 0.1 mm. The first precise measurements with beams indicated that the LEP circumference was in fact more than twice as precise as predicted: better than 1 cm in 26.67 km.

1.1.3 The magnet and power-converter systems

The electromagnetic guide field system of LEP consists of dipoles, quadrupoles, sextupoles, horizontal and vertical dipole correctors, rotated quadrupoles, and finally electrostatic dipole deflectors. About three quarters of the LEP circumference is occupied by 'standard cells'. Each of the eight arcs composing the ring contains 31 of these standard cells, which are comprised of magnets in the following order: a defocusing quadrupole, a vertical orbit corrector, a group of six bending dipoles, a focusing sextupole, a focusing quadrupole, a horizontal orbit corrector, a second group of six bending dipoles, and finally a defocusing sextupole. The length of a standard cell is 79.11 m.

The electrons and positrons are bent in a piecewise circular trajectory by the strings of dipole magnets. The bending field of these dipoles has been made unusually low (about 0.1 T) so as to increase the bending radius and thereby reduce the amount of synchrotron radiation. The quadrupole magnets, which produce fields linear with the transverse position, act as magnetic lenses and focus the beam to be comfortably contained within the vacuum chamber. The alternating polarity of the quadrupoles in the standard cells produces alternating-gradient focusing or 'strong' focusing. The cell sextupoles produce a field which is quadratic in transverse displacement, and they are used to compensate the dependence of the focusing strength on the beam energy ('chromaticity'). The small horizontal and vertical correctors are individually powered so as to allow 'steering' of the beam through the centre of the LEP aperture.

Each experimental collision point in LEP is surrounded by a large solenoidal magnet used for particle identification. The bunches of each beam must be tightly focused ('squeezed') to very small dimensions in the centre of these detectors in order to increase the luminosity or particle production rate. This is accomplished by a set of superconducting quadrupoles with very strong field gradients that focus the transverse beam dimensions to about 10 μm and 250 μm in the vertical and horizontal planes respectively. The solenoidal detector magnets produce another effect, however: they cause the horizontal oscillations to be 'coupled' into the vertical plane; if this were uncompensated it would greatly increase the vertical beam size and cause a reduction in the luminosity. For this reason, rotated quadrupoles are installed around each solenoid to compensate this magnetic coupling. These quadrupoles are similar to conventional quadrupoles but rotated about their axis by 45 degrees.

The strengths of all magnets in the LEP ring are very accurately adjusted by controlling the current flowing in their coils. This is accomplished by the use of more than 750 precisely stabilized d.c. power supplies ranging from less than 1 kW to a maximum of 7 MW. The specifications for these power supplies are extremely tight, both in their individual operation and, during energy ramping, in their precise synchronization. For the main dipole and quadrupole supplies, absolute accuracies down to 2 parts in 10^5 have been achieved with a resolution typically three times better.

Each magnet has its own cooling circuit. For the majority, the cooling is provided by demineralized water circuits, which are connected to a total of 10 cooling towers with a capacity of 10 MW each. Some of the small corrector magnets are air-cooled, whilst the superconducting quadrupoles and the superconducting experimental solenoids are cooled by liquid helium at 4.2 K from the cryogenics installation.

1.1.4 The acceleration system

The RF acceleration system installed at present includes 128 five-cell copper cavities powered by sixteen 1 MW klystrons via a complex of waveguides and circulators. Each accelerating cavity is coupled to a spherical low-loss storage cavity in such a way that the electromagnetic power continuously oscillates between the two sets of cavities. The coupling is arranged so that the power is at its peak in the acceleration cavities at the instant of the passage of the beam bunches. In this way, the bunches receive the maximum possible accelerating gradient, but the power loss due to heating of the copper cavity walls is greatly reduced since the electromagnetic power spends half of its time in the very-low-loss storage cavities. The operating frequency is 352.21 MHz, which corresponds to 31,320 times the revolution frequency of a beam circulating in LEP. The present system allows for a peak RF voltage of 400 MV per revolution.

The sinusoidal electric field that is generated in each accelerating cavity cell produces a 'potential well', inside which each particle of each bunch can perform stable oscillations with respect to the particle at the centre of the bunch, i.e. the synchronous particle. These oscillations are around the energy of the synchronous particle and, in azimuthal distance, ahead of or behind this particle. When represented in a phase-plane plot of normalized energy as a function of normalized distance, the trajectories form circles for the case of small oscillation amplitudes while the maximum stable oscillation possible inside the potential well forms a closed contour (the RF bucket). There can possibly be as many synchronous particles and hence stable regions (buckets) as there are RF oscillations in the revolution time of LEP. As previously stated, this means a total of 31,320 buckets for LEP, with the possibility of stable oscillations in each. However, in order that the e^+e^- bunches collide at the centres of the experimental detectors, they must be injected and accumulated in precisely the correct buckets. This is achieved by a very precise synchronization system between the RF systems of LEP and its injector, the SPS.

1.1.5 The beam instrumentation

The LEP beam instrumentation system is used to observe the position, shape, or other relevant properties (such as polarization or electrical current) of the beam. A simple way to observe the beam is by placing a monitor directly in the path of the primary beam: an example of this is the luminescent screen that is used to observe the position and shape of the injected beam. The beam particles interact with the chromium in the screen and produce a luminescent image of the cross section of the beam which is transmitted as a television signal to the control room. The beam electrical current is measured in LEP as in other accelerators by current transformers placed around the vacuum chamber. These transformers are capable of measuring the current of a single injection or of a steady circulating beam. In the latter case the beam lifetime can be evaluated by accurate measurement of the current as a function of time.

When charged particles are bent in a circular trajectory they radiate photons. Consequently, the beams can be 'seen' by measuring this flux in the ultraviolet (UV) frequency range. Four UV monitors are used in LEP to measure the transverse dimensions of both beams at two different locations. The images are transmitted to the control room to give a real-time view of the beam, while the digital signals are processed to provide numerical values for the beam sizes.

The synchrotron radiation results in another problem: background originating from the high-energy spectrum of the photon emissions. In order to reduce this background, collimators are installed around each experimental point. Each of these collimators consists of remotely movable jaws of tungsten and copper, which can intercept and absorb the high-energy photons. Since these collimators can be placed very close to the beam, they were designed to accommodate, inside each horizontal jaw, a mini-calorimeter consisting of tungsten absorbers and silicon detectors. These mini-calorimeters are used to measure the relative luminosity in each experimental point by counting the number of Bhabha events at very small angles to the beam trajectory. In addition, other collimators are located far from all the experiments: these define the LEP aperture and remove any beam halo that might otherwise end up in one of the detectors. The system of collimators has proved invaluable in LEP and has resulted in low background conditions in the detectors practically from the first physics run.

1.1.6 The vacuum system

The duration of a typical operation to fill LEP with particles for a physics run is 12 hours. During this time each of the 10^{12} particles in the beams will have traversed the complete 26.67 km of the LEP vacuum chamber about 500 million times. In order to minimize particle losses due to collisions with residual gas molecules, the whole vacuum chamber must be pumped down to very low pressures. The achieved static pressure for LEP is $8 \cdot 10^{-12}$ $Torr$ whereas in the presence of beam the pressure rises to about 10^{-9} $Torr$. This pressure rise is due to gas desorption from the inner vacuum-chamber wall, provoked by the synchrotron radiation of the circulating beam.

The two main components of the vacuum system are the vacuum chamber itself and the pumping system. Of the 27 km of LEP vacuum chamber, a length of about 22 km passes through the dipole and quadrupole magnets, and is subject to the heating due to synchrotron radiation. Although this heating represents a mere 100 W/m for phase 1, it rises to more than 2000 W/m for phase 2. Therefore the chambers need water-cooling channels and are constructed from aluminium because of its good thermal conductivity. However, only about half the radiated power would be absorbed by the aluminium; the remainder would normally escape into the tunnel, which would produce highly corrosive nitric acid in the presence of humid air. For this reason, the aluminium chamber is covered with a lead cladding of a thickness varying between 3 and 8 mm, which greatly reduces the radiation that escapes into the tunnel during operation. Other types of chambers are used in special regions such as the injection, RF, electrostatic separators, and the detector regions. For the main part these are made of stainless steel except for the detector regions where, for reasons of transparency to particles, they are fabricated from beryllium, thin-walled aluminium, or carbon-fibre composites.

For reasons of reliability the 26.7 km of the LEP vacuum system is subdivided into smaller 'vacuum sectors' with a maximum length of 474 m. During shutdown periods, when there is no circulating beam and work is often going on in the tunnel, these vacuum sectors are isolated from each other by full-aperture gate vacuum 'sector valves'. Consequently, if an accident occurs, only 474 m of vacuum will be affected and not the full 26.7 km.

1.1.7 Injectors and pre-injectors

The LEP storage ring is the last accelerator in a chain of five, each of which handles the same electrons and positrons generated on every pulse by the electron gun and the positron converter (fig. 1.1).

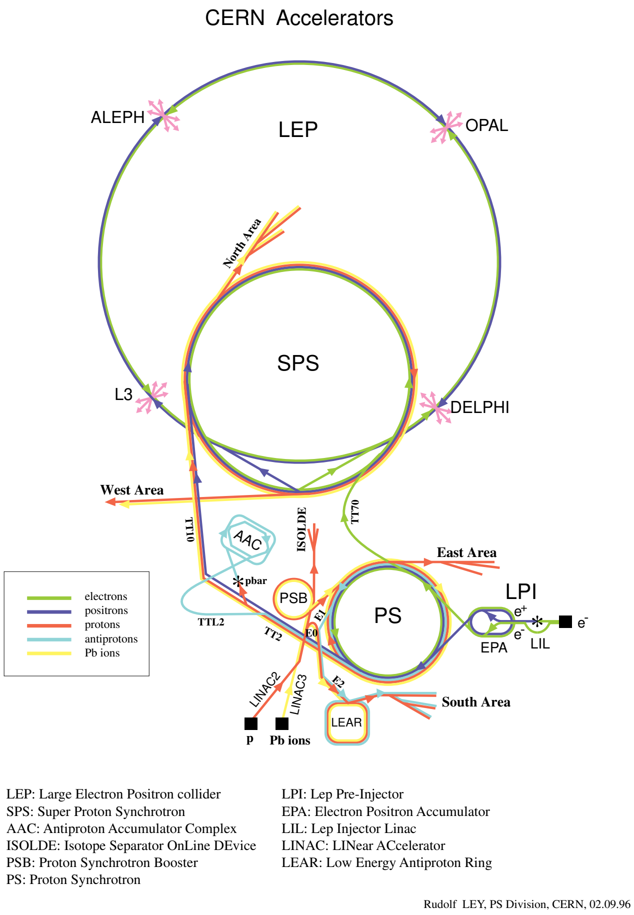

Figure 1.1: *The CERN accelerator system*

The LEP injectors consist of two linacs of 200 MeV and 600 MeV followed by a 600 MeV Electron-Positron Accumulator (EPA), which injects into the CERN Proton Synchrotron (PS) operating as a 3.5 GeV e^+e^- synchrotron. The PS then injects into the CERN Super Proton Synchrotron (SPS), which operates as a 20 GeV electron-positron injector for LEP. The decision to use the two already existing CERN proton synchrotrons (the SPS and the PS) and all the infrastructure associated with them, resulted in significant economies both in cost and in time. The PS, originally designed for 28 GeV protons and commissioned in 1959, was modified to allow acceleration of electrons and positrons from 600 MeV to 3.5 GeV. The SPS, designed to accelerate protons to 450 GeV and first brought into operation in 1976, was modified to accept electrons and positrons from the PS at 3.5 GeV, accelerate them to 20.0 GeV, and finally transfer them to the LEP collider. In order to serve LEP with electrons and positrons, both the PS and the SPS operate in multicycle mode. In this mode, a supercycle is used which incorporates four cycles of electrons/positrons followed by one cycle of protons. Consequently, owing to the fact that the electrons/positrons are accelerated in the dead-time between the proton cycles, the filling of LEP has had little or no effect on the 450 GeV SPS stationary-target physics, which runs in parallel.

1.2 The DEtector with Lepton, Photon and Hadron Identification

The electrons and positrons accelerated by LEP are allowed to meet in the center of DELPHI. This is a general purpose detector with special emphasis on particle identification, three-dimensional information and precise vertex determination. It is placed in a cavern 100 m below ground. It consists of a central cylindrical (or 'barrel') section and two end-caps (or 'forward' sections) (fig. 1.2). The radius is about 5 m and the length is over 10 m. The inner components are enclosed by a superconducting coil, providing a uniform 1.2 T magnetic field.

A description of the subdetectors is given below, where we address the components that are relevant to this analysis more extensively.

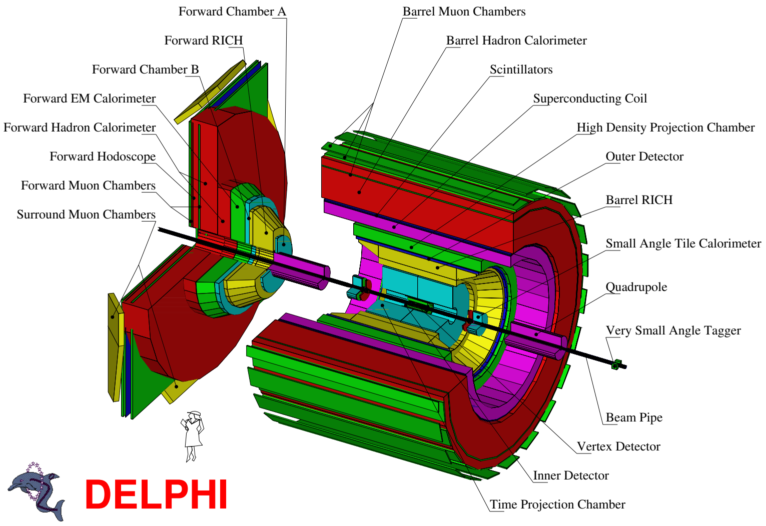

Figure 1.2: *The DELPHI detector.*

1.2.1 Tracking

Apart from the Silicon Tracker and the Time Projection Chamber, that we describe below, the tracking system of DELPHI comprises the following components:

- the Inner Detector (ID): it is shown as the smallest green cylinder in fig. 1.2. It is located between the Vertex Detector and the Time Projection Chamber and provides intermediate precision position and trigger information. It consists of two parts: the JET chamber and the Trigger Layers (TL). The JET chamber is a drift chamber subdivided into 24 sectors of 15 degrees in ϕ. It provides up to 24 $R\phi$ points per track between radii of 12 and 23 cm. The polar angle coverage extends down to 15 degrees. The TL consists of five cylindrical multiwire proportional chambers giving fast trigger information and z-information for charged tracks. The JET chamber accuracy is of the order 40 μm in $R\phi$ and 1.2 $mrad$ in ϕ.

- the Outer Detector (OD): it is shown as the narrow dark blue cylinder in fig. 1.2. It consists of 24 modules containing five layers of drift tubes located between radii of 197 and 206 cm. The active length of the detector corresponds to polar angles from 42 to 138 degrees. The detector is important for the precision of the momenta of charged particles measured by the TPC. It provides three space points plus two $R\phi$ points per track. For each tube in the detector, the drift distance of the produced electrons is derived from their drift time. All the tubes in the 3 internal layers give a z value. The precision over the measure of the $R\phi$ coordinate is 100 μm per track. The accuracy of the z measurement is of 4.4 cm. The detector is also used for trigger information. ID and OD correlated trigger data are used in order to reduce the rate due to cosmic and beam gas events.

- the Forward Chambers (FCA and FCB): the FCA is shown as the smaller blue component in the forward part in fig. 1.2. It is distant from the interaction point of about 160 cm in z. It provides tracking and trigger information at polar angles from 11 to 32 degrees and from 148 to 169 degrees. The FCB is shown as the bigger blue component in the forward part in fig. 1.2. It is a drift chamber at an average distance of 275 *cm* from the interaction point. The sensitive area of the chamber corresponds to polar angles from 11 to 36 degrees and from 144 to 169 degrees.

- the Muon Chambers (Barrel, Forward and Surrounding): they are farthest the collision point, since muons are the only charged particles that can traverse the lead and iron of both calorimeters essentially unaffected. Most muons of momenta above 2 GeV are expected to penetrate to the Muon Chambers. Muon identification is achieved by comparing the extrapolations of the reconstructed tracks with the hits in the Barrel (MUB, which covers polar angles from 53 to 89 degrees and from 91 to 127 degrees) and Forward (MUF, which covers polar angles from 20 to 42 degrees and from 138 to 160 degrees) muon drift chambers. In 1994 a layer of Surrounding Muon Chambers (SMC) was installed outside the endcaps to fill the gap between the barrel and forward regions.

1.2.1.1 The Silicon Tracker (VD, VFT)

The Vertex Detector (VD) is located nearest the collision point. Its main objective is to provide an accurate measurement of the $R\phi$ coordinate close to the interaction point, improving the reconstruction of the primary vertex and enabling secondary vertices reconstructions from decays of heavy quark flavours.

The old VD has been upgraded for LEP200: the barrel length has been doubled from 24 to 48 *cm* and is now the barrel part of the Silicon Tracker. It consists of tree coaxial cylindrical layers of AC coupled silicon strip detectors at average radii of 6.3, 9.0 and 10.9 *cm* (fig. 1.3). At present the polar angle coverage extends down to 25 degrees.

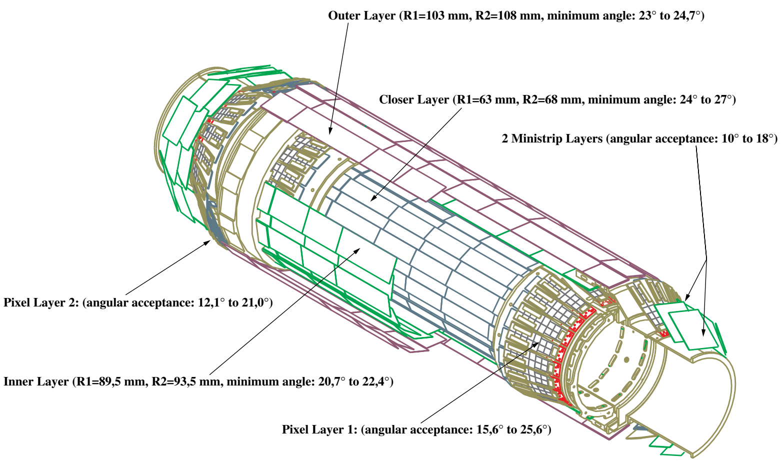

Figure 1.3: *The Silicon Tracker of DELPHI.*

The Very Forward Tracker (VFT) is located on both sides A and C of the new 1996 vertex detector. On each side it is built from two layers of mini strip and two layers of pixel detectors. It covers the polar angle from 10 to 25 degrees and from 155 to 170 degrees. The VFT is the forward part of the Silicon Tracker.

1.2.1.2 The Time Projection Chamber (TPC)

The Time Projection Chamber is shown as the big blue cylinder in fig. 1.2. It is the principal tracking device of DELPHI. It also helps in charged particle identification by measuring the dE/dX. It is a cylinder of 2x130 *cm* situated between the radii 29 *cm* and 122 *cm* (fig. 1.4). The detector provides points per particle trajectory at radii from 40 to 110 cm between polar angles from 39 to 141 degrees. At least three pad rows are crossed down to polar angles from 20 to 160 degrees.

The two drift volumes are separated by a HV (20 kVolts) plate producing an electric field of 150 $Volts/cm$. A charged particle crossing the TPC produces by ionisation around 70 electrons per cm of gas (80 % Ar and 20 % CH_4). Under the action of the electric field these primary electrons drift in the direction of the proportional chambers (6 at each TPC extremity). Each of 2x6 TPC sectors have 16 raws of pads, allowing the reconstruction of 16 space points per track. In front of the pads plates there

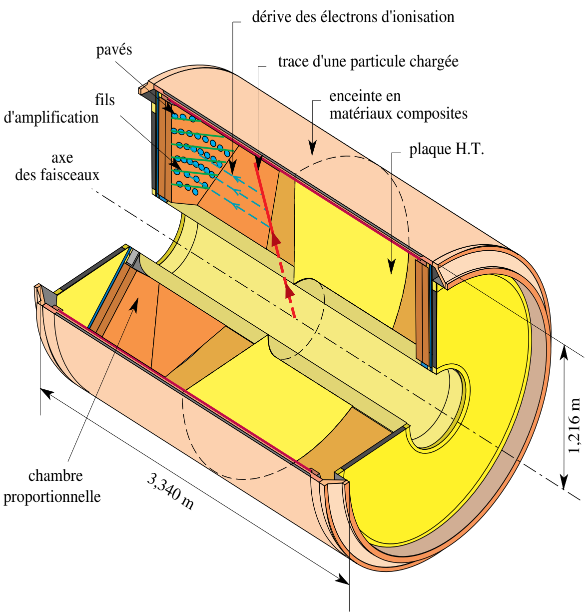

Figure 1.4: *The Time Projection Chamber of DELPHI.*

are 3 levels of grid. The one closest to the pad (the anode at a HV of 1430 Volts) contains 192 "active" wires (sensitive wires) per sector performing the dE/dx measurement.

The precision over the measure of the $R\phi$ coordinate is 250 μm per point. The accuracy of the z measurement is of 900 μm per point.

1.2.2 Electromagnetic calorimeters

Electron and photon identification is provided primarily by the electromagnetic calorimetry system. It is composed of a barrel calorimeter (HPC), a forward calorimeter (FEMC) and two very forward calorimeters, the Small angle TIle Calorimeter (STIC), which replaced the Small Angle Tagger (SAT) in April 1994, and the Very Small Angle Tagger (VSAT). The latter two are used mainly for luminosity measurements and are described in section 1.2.5.

- the High-density Projection Chamber (HPC): it is shown as the big green cylinder in fig. 1.2. Its length is 2x254 cm and it is situated between the radii 208 cm and 260 cm. The polar angle coverage is from 43 to 137 degrees. The granularity is 1 degree in ϕ, 4 mm in z and 9 samples in R. It consists of 144 independent modules, arranged in 6 rings of 24 modules each. Each HPC module is a trapezoidal box with a width ranging from 52 to 64 cm and a height of 47 cm. The length is 90 cm, except for modules in the first and last rings which are somewhat shorter. The box is filled with 41 layers of lead separated by gas gaps (8 mm each, filled with 80% argon and 20% methane). An electromagnetic particle showers in the lead and ionizes the gas. The charge drifts to one end of the box, where it is collected by a proportional chamber. The electric and magnetic fields are precisely aligned by adjusting the orientation of each box, making it possible for the ionization electrons to spiral all the way to the readout chamber. With a drift speed around 5.5 $cm/\mu s$, the maximum drift time is 16 μs. The 10th sampling gap at about 4.5 radiation lengths (shower maximum) is filled with a scintillator plane instead of gas. It is used for the first level trigger.

- the Forward ElectroMagnetic Calorimeter (FEMC): it is shown as the green disk component in the forward part in fig. 1.2. It consists of two 5 m diameter disks made of 4532 Cherenkov lead glass blocks. The front faces are placed at $z = \pm 284\ cm$, covering the polar angles from 8 to 35 degrees and from 145 to 172 degrees. The operation of lead-glass Cherenkov counters is based on the collection of Cherenkov light emitted by the charged tracks of a shower. If n is the refractive index of the medium traversed by a particle and β its speed in units $c = 1$, part of the light emitted by excited atoms appears in the form of a coherent wavefront at fixed angle with respect to the trajectory ($cos(\theta) = 1/(\beta * n), \beta > 1/n$). The pulse height is related to the number of photoelectrons knocked out of the photocathode by the Cherenkov light. The Cherenkov signal induced by the charged particles in the shower is read out by a single stage photomultiplier designed to operate inside the DELPHI magnetic field, coupled to a low noise preamplifier. The average yield of photoelectrons is about 1000 per GeV of deposited energy. The relative precision on the measured energy can be parametrised as : $\sigma(E)/E = 0.03 + (0.12/\sqrt{E}) + (0.11/E)$, where E is in GeV. For neutral showers of energy larger than 2 GeV, the average precision on the reconstructed hit position in x and y projected to $z = \pm 284\ cm$ is about 0.5 cm.

The hadron calorimeter (HACL) is shown as the red component in fig. 1.2. It is a sampling gas detector incorporated in the magnet yoke (it consists mainly of iron), the barrel part covering polar angles from 42.6 to 137.4 degrees, and two end-caps from 11.2 to 48.5 degrees and from 131.5 to 168.8 degrees. The hadron calorimeter provides calorimetric energy measurements of charged and neutral hadrons. In addition is implemented a system to read out the HACL tubes as well as the pads, in order to give a more detailed picture of the hadronic showers and thus better distinction between showers caused by neutral and charged hadrons and better muon identification.

1.2.3 Scintillator counters

In order to achieve complete hermeticity for high energy photon detection, additional scintillators have been installed in the cable duct regions (between the barrel and each endcap, and between the HPC modules), the HERmeticity detectors (HER). In addition the DELPHI has in the barrel part the Time Of Flight (TOF) and in the forward part the HOrizontal Flight tagger (HOF). The scintillator counters are also fast trigger for beam events and cosmic radiation.

1.2.4 Particle identification

The identification of charged hadrons in DELPHI relies on the specific ionization energy loss per unit length (dE/dX) in the TPC and on the RICH detectors. The RICH technique is based on the detection of Cherenkov light emitted by the particle. The DELPHI RICH contains two radiators of different refractive indices. The liquid radiator is used for particle identification in the momentum range from 0.7 to 9 GeV. The gas radiator is used from 2.5 to 25 GeV. The full solid angle coverage is provided by two independent detectors, one in the endcap regions (Forward RICH), and one in the the barrel regions (Barrel RICH).

The Barrel RICH Detector (Barrel-RICH) is shown in yellow in fig. 1.2. It is located between the Time Projection Chamber and the Outer Detector. It is a 350 cm long cylinder with inner radius 123 cm and outer 197 cm, divided into two halves by a central support wall, 6.4 cm thick. It covers polar angles between 40 and 140 degrees.

The Forward RICH Detector (Forward-RICH) is shown as the yellow disk component in the forward part in fig. 1.2. It is located between $1.7\ m < |z| < 2.7\ m$ and covers polar angles between 15 and 35 degrees.

1.2.5 Luminosity measurement

At e^+e^- colliders, luminosity is measured by counting the number of events of a process with a clear experimental signature, with high statistics and with a cross section which can be calculated theoretically with high precision. This process is Bhabha scattering at small angles, which proceeds almost entirely through the exchange of a photon in the t-channel. In DELPHI there are two luminometers: the Small angle TIle Calorimeter (STIC) and the Very Small Angle Tagger (VSAT).

1.2.5.1 The Small angle TIle Calorimeter (STIC)

At the beginning of 1994 the DELPHI collaboration installed a new electromagnetic calorimeter named STIC (Small angle TIle Calorimeter) [2], [3], [4], [5] with the aim of providing a luminosity measurement with an accuracy of 0.1 % at LEP1.

The luminometer consists of two lead-scintillator cylindrical calorimeters of shashlik type, read out by wavelength-shifting fibers. These are located on either side of the interaction point at a distance of 2.2 m. They cover the angular region between 29 and 185 $mrad$ in polar angle (fig. 1.5).

Each of the calorimeters is equipped with two planes of silicon-strip detectors with which the direction of a shower can be measured. The purpose of this tracking device is to improve the rejection of off-energy

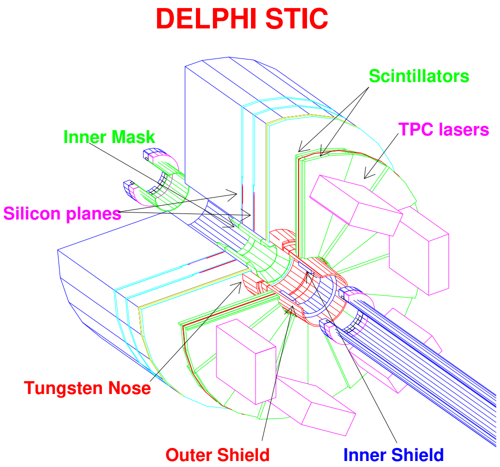

Figure 1.5: *The Small angle TIle Calorimeter.*

electron background. A veto system consisting of two layers of scintillators is mounted in front of each arm of STIC. This veto system is part of the neutral trigger. This trigger is aimed at selecting single-photon events in STIC. It provides $e-\gamma$ separation by requiring an energy deposit in one of the two STIC calorimeters in conjuction with an absence of signals in the scintillator planes in front of the calorimeters.

Several tungsten masks and shields are mounted on and near STIC. A so-called tungsten nose is mounted on the front face of the calorimeter on side C (but not on side A) and is used to define the acceptance for Bhabha electrons in luminosity measurements. A synchrotron radiation mask is mounted underneath each arm of STIC, inside the beam pipe, and these masks protect the DELPHI TPC from synchrotron radiation. Furthermore, a 'tungsten shield', mounted on the tungsten nose, provides additional radiation protection to the TPC.

Each calorimeter is divided into 10 radial rings and 16 azimuthal sectors, thus giving a total of 160 towers which point to the interaction region.

The energy resolution at 45 GeV is 3%. The spatial resolution of the calorimeter alone is 1.5 degrees in ϕ and from 300 μm to 1 mm in radius. The resolution of the silicon strips (1.7 mm pitch) over the measure of radial coordinate is 400 μm.

1.2.5.2 The Very Small Angle Tagger (VSAT)

The VSAT [6] is shown as the small green boxes in fig. 1.2. It is a sampling calorimeter consisting of four rectangular modules placed symmetrically at about 7.7 m from the DELPHI origin, around a short elliptical section of the beam pipe downstream the low beta superconducting quadrupoles (SCQ) as shown in fig. 1.6. The distance between two neighbouring modules is about 12 cm, corresponding to the smaller beam pipe dimension in that region. Since the physical process studied for the luminosity measurement is Bhabha scattering, where electrons and positrons are emitted back to back, we use the coincidences of signals between a module in the forward region and a module in the backward region, thus defining two diagonals for the trigger: diagonal 1 (modules F1-B2) and diagonal 2 (modules F2-B1).

Each VSAT module contains 12 tungsten absorbers ($X_0 = 0.38$ cm) interspaced with 12 silicon planes (Full Area Detectors, (FAD)) for energy measurement (fig. 1.7). The dimensions of the calorimeters are 3 cm in the transverse horizontal direction (x), 5 cm in the vertical direction (y) and 24 radiation lengths (about 10 cm) along the beam direction (z). The center of the electromagnetic shower is given by three silicon strip planes with 1 mm pitch placed close to the shower maximum at 5, 7 and 9 r.l.; the second plane is used for the y coordinate measurement and the other two planes for the x coordinate measurement. The angular acceptance of a module is 5-7 mrad in polar angle and $\pm$ 50 degrees in azimuth.

Due to the very small emission angle of the Bhabha events accepted in the VSAT, the accepted Bhabha cross section is very large (about 500 nb). This allows to monitor with high statistics, besides the luminosity, also the beam background and the variation of beam parameters.

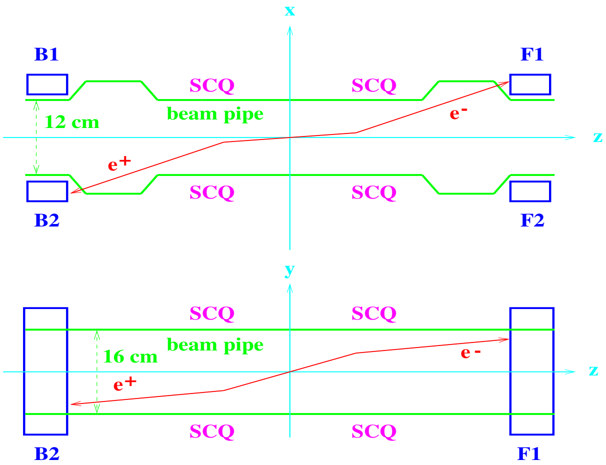

Figure 1.6: *Layout of the position of the VSAT modules in the (x,z) and (y,z) planes.*

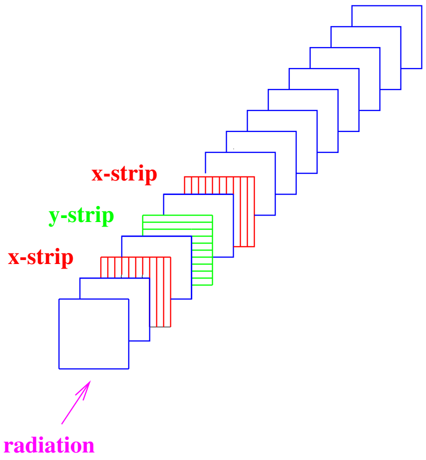

Figure 1.7: *Structure of the VSAT modules.*

Chapter 2

Luminosity

After the beam energy, the most important parameter at a colliding beam facility is the counting rate [7]. This is usually expressed by the term luminosity, which we define below. We will also discuss the expressions which allow the collider builder to know what the luminosity will be in terms of his machine parameters. Once the machine is built and operating the high energy physicist needs to know the machine luminosity in order to be able to normalize his measurements and he usually requires a more accurate value than what can be obtained directly from machine parameters. We will therefore also discuss an indirect method of measuring luminosity.

2.1 Definition of luminosity

For simplicity we first consider the interaction of a beam with a target of length l and particle number density n_2, as sketched in fig. 2.1.

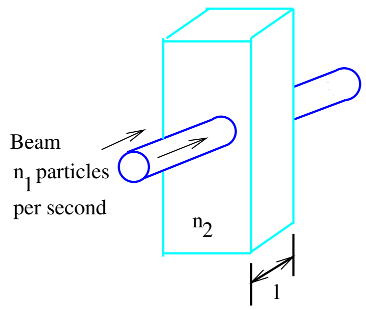

Figure 2.1: *Schematic of a particle beam of n_1 particles per second incident on a stationary target with n_2 particles per unit volume.*

The number of interactions, R, per beam particle is proportional to $n_2 \cdot l$, the total number of particles it can collide with and the constant of proportionality is defined as the cross section q for the type of interaction concerned

$$R = q n_2 l$$

where q has the dimension cm^2. The transverse dimensions of the beam and target do not enter as the target is assumed to be wider than the beam. If the beam consists of n_1 particles per second, the rate of interactions will be

$$\frac{dR}{dt} = q n_1 n_2 l.$$

All the characteristics of the incident beam and target can be combined into a single term defined as the luminosity L by writing

$$\frac{dR}{dt} = qL \tag{2.1}$$

where $L = n_1 n_2 l$ and has the dimensions $cm^{-2}s^{-1}$. Hence luminosity is simply the interaction rate per unit cross section.

2.2 Luminosity of a single-ring collider

In a colliding beam machine the expression for L is more complicated because the target is moving and we cannot always assume that the target is wider than the beam.

We consider an electron-positron collider with $N_{-,+}$ particles per beam. The number of positrons one electron encounters in one turn of the machine, assuming the beams follow identical paths, is

$$\frac{q}{A}N_+$$

where q is the effective cross section of the electron and A is the cross sectional area of the beams. With N_- electrons in the beam and a revolution frequency of f, the interaction rate will be

$$\frac{dR}{dt} = \frac{q}{A}N_+N_-f$$

If we have B bunches in each beam, the interaction rate per crossing is given by

$$\frac{dR}{dt} = \frac{N_+N_-fq}{BA}$$

In most storage rings the transverse particle distribution is gaussian or bell shaped and since only the core of the beam contributes significantly to the luminosity we may define standard beam sizes for all kinds of particles [8]. For a gaussian particle distribution the effective beam cross section is

$$A = 4\pi\sigma_x\sigma_y$$

supposing that the beams have equal r.m.s. radii of σ_x (horizontal) and σ_y (vertical). Then

$$\frac{dR}{dt} = \frac{N_+N_-fq}{4\pi B\sigma_x\sigma_y}$$

and the luminosity

$$L = \frac{N_+N_-f}{4\pi B\sigma_x\sigma_y} \tag{2.2}$$

In terms of the currents, $I_{+,-} = N_{+,-}ef$, the luminosity is given by:

$$L = \frac{I_+I_-}{4\pi e^2 B\sigma_x\sigma_y f}.$$

The transverse dimensions of the beams (σ_x and σ_y) can be expressed in terms of two machine parameters: the emittance, $\epsilon_{x,y}$, which is a measure of the area of the phase space ellipse occupied by the beam and $\beta_{x,y}$, reflecting the strength of the machine optics, through the relations

$$\sigma_{x,y} = \sqrt{\epsilon_{x,y}\beta_{x,y}}$$

$$k = \frac{\epsilon_y}{\epsilon_x}$$

where k is the coupling between the vertical and horizontal emittance. Thus

$$L = \frac{I_+I_-}{4\pi e^2 B\sqrt{k\beta_x\beta_y}\epsilon_x f}. \tag{2.3}$$

With typical LEP conditions [9]

$$N_{+,-} = 1.3\cdot 10^{12}$$

$$f = 11.25\,kHz$$
$$B = 4$$
$$\beta_x = 175\,cm$$
$$\beta_y = 7.5\,cm$$
$$k = 0.05$$
$$\epsilon_x = 35\,nm,$$

the LEP luminosity becomes $L \approx 10^{31}\,cm^{-2}s^{-1}$.

For a given experiment one defines also the integrated luminosity

$$\overline{L} = \int L dt$$

which depends upon the life-times of the beams, the filling time and the duration of the experiment [10].

The recipe for high luminosity is clearly to maximize the beam intensity and to minimize the beam cross section. This approach, however, is limited by two phenomena: the synchrotron radiation and the beam-beam effect.

2.2.1 Synchrotron radiation

Under the circular acceleration, an electron emits synchrotron radiation, the energy radiated per particle per turn being [11]

$$\Delta E = \frac{4\pi}{3}\frac{e^2\beta^2\gamma^4}{\rho}$$

where ρ is the bending radius, β is the particle velocity and $\gamma = (1-\beta^2)^{-1/2}$.

The loss of momentum due to the emission of photons is parallel and opposite to the direction of the particle momentum [12]. Since the particles perform betatron oscillations, the momentum loss can be split into a transverse and longitudinal component. The accelerating fields, on the other hand, provide a compensation of the lost momentum only in the longitudinal direction. In total the emission of synchrotron radiation eventually leads to a continuous loss of transverse momentum, which in turn sets a limit on the number of particles available in a bunch.

2.2.2 Beam-beam effect

The beam-beam [8] effect consists in the interaction between the beams and the electromagnetic fields created by them in the vacuum envelope. It has two consequences: first, it sets a maximum to the number of allowable particles in the bunches; second, it imposes a minimum to the beam cross section.

The limitation on the amount of beam that can be brought into collision stems from the tune shift caused by the beam-beam interation. For two counter rotating beams of particles and antiparticles there is a vertical beam-beam force of

$$F_y = -\frac{e(1+\beta^2)2\lambda}{\sigma_y(\sigma_x+\sigma_y)}y.$$

This force is attractive and therefore focusing, equivalent to that of a quadrupole of length

$$k = -\frac{F_y/y}{c^2\beta^2\gamma m}$$

causing a vertical tune shift of

$$\delta\nu_y = \frac{1}{4\pi}\int_{coll}\beta_y k ds.$$

Integrating over the collision length which is equal to half the bunch length l because colliding beams move in opposite directions, we note that the linear charge density is $\lambda = eN/B/l$, where n is the total number of particles per beam and B the number of bunches per beam. With these replacements the beam-beam tune shift becomes finally

$$\delta\nu_y = \frac{r_0 N \beta_y}{2\pi B \sigma_y(\sigma_x + \sigma_y)},$$

where r_0 is the classical particle radius of that particle which is being disturbed. Obviously, the tune shift scales linearly with particle intensity or particle beam current and inversely with the beam cross section.

2.3 Online measurement of the luminosity

The ability to get a good estimate of the achieved luminosity at run time is essential both for the experiment and for the accelerator [13]. The VSAT detector uses the so called MIG scalers to evaluate the online luminosity [14]. For this purpose the ungated Bhabha and false Bhabha counters are used:

$$L = const \cdot (BHUNG1 - FBUNG1 + BHUNG2 - FBUNG2)$$

The constant contains information about the accepted Bhabha cross section, which varies with the running conditions. For the online luminosity, the statistical fluctuations during the short time intervals, i.e. 15 seconds, used to evaluate the trigger rate are more significant and instead an average value of the accepted cross section is used. The measurement is also normalized to the STIC online luminosity. This normalization usually has to be redone every year due to shifts in the geometry, which affect the relative accepted cross section in a non negligible way. The VSAT online luminosity is displayed together with the STIC values as a traceplot in the DELPHI control room. We give an example plot of LEP luminosity for a fill taken on 14/09/97 at 183 GeV. The accuracy of the calculation is a few percent.

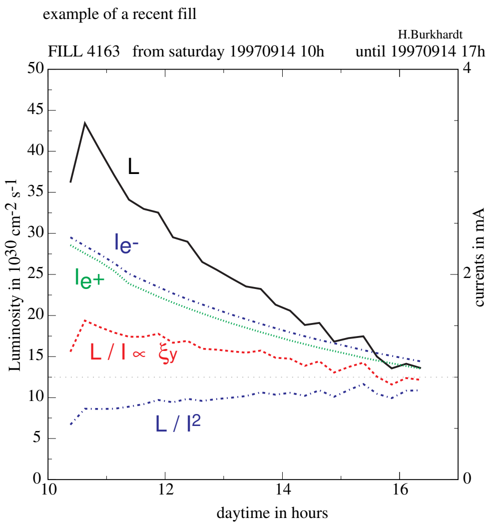

Figure 2.2: *Online luminosity for LEP. The values are averages for the four experiments.*

2.4 Offline measurement of the luminosity

In principle, eq. (2.3) implies that the luminosity is known provided the transverse beam dimensions can be measured [7]. In practice, while machine designers make use of such expressions, at an operating collider the experimenters require a more precise knowledge of the luminosity for normalization purposes and must find other means. At an electron machine the standard technique is to set up a monitor consisting of small-angle electron telescopes to observe elastic (Bhabha) scattering as in fig. 2.3.
This process has a well known cross section σ_B, so that from a measurement of the counting rate the luminosity can be determined using eq. (2.1). The cross section, σ, must of course be calculated for the acceptance of the detector

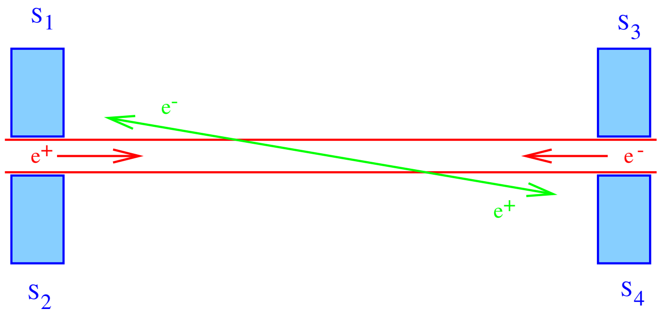

Figure 2.3: *Layout of a typical luminosity monitor to detect Bhabha scattering at electron-positron storage rings.*

$$\sigma = \int_{\theta_{min}}^{\theta_{max}} \frac{d\sigma_B}{d\Omega} d\Omega$$

where θ_{min} and θ_{max} are the minimum and maximum scattering angles accepted by the monitor. We give the expression of the cross section in the next chapter.

Chapter 3

Bhabha Scattering

By elastic Bhabha scattering [15] one means the process

$$e^+e^- \rightarrow e^+e^- \tag{3.1}$$

where only an e^+e^- pair is detected in the final state. It is a relevant process at LEP I for luminosity monitoring, line shape and $A^e_{FB} = \frac{\sigma^F - \sigma^B}{\sigma^F + \sigma^B}$ measurements, where σ^F (σ^B) is the Bhabha cross section for the production of an electron with $cos\theta > 0$ ($cos\theta < 0$) and θ is the angle of the outgoing electron with respect to the incident electron direction. In this chapter, we give a general discussion of the process including formulae for the lowest order differential cross section. The electroweak radiative corrections are briefly discussed at one-loop level. Finally, the Born cross section for very small angles is given, i.e. at the polar region covered by the VSAT.

3.1 The 'real' Bhabha scattering

Strictly speaking, the process (3.1) never occurs; as required by classical electrodynamics, a charged particle must emit, when scattered, some amount of electromagnetic radiation, so that in an actual scattering event the final state contains also photons in addition to the electron-positron pair. Such radiation effects become increasingly important as energy increases.

The electromagnetic radiation is emitted within a collinearity cone, whose opening angle shrinks as energy increases as m/E, where m is the electron mass and E its energy. At LEP, $m/E \approx 10^{-5}$ so the photons radiated by the incoming particles remain undetected within the beam pipe.

Like most of the real, detectable LEP processes, a Bhabha event can be depicted as occuring in three steps:

(i) emission of radiation from the initial particles;

(ii) the 'hard', elastic Bhabha scattering;

(iii) emission of radiation from the final particles.

For the purpose of the step (ii) above, the scattering can be considered 'hard' if the scattering angle θ is larger than the collinearity angle m/E, a condition easily fulfilled at LEP (even luminosity monitors will not go to angles less than a few mrad). In such conditions, interference effects between initial and final particles in the emission of radiation can be safely ignored. Also, due to the strong collinearity, step (ii) can be considered as occuring between particles on the mass shell.

As far as the energy-momentum of the radiation emitted in step (iii) by the final particles is not experimentally resolved from the particles themselves, the experimental results must be compared with the theoretical prediction for the process inclusive of the emission of radiation.

In the cms, all four particles involved in a fully elastic Bhabha scattering have the same energy E. Due to step (i), the laboratory is no longer the cms for step (ii) and the process is therefore initiated by particles of non equal energies E_1^0, E_2^0, both smaller than the beam energy E_b, negligable transverse momentum and non vanishing total longitudinal momentum, as in general $E_1^0 \neq E_2^0$ for any specific event. As a consequence, the final observed particles, or rather the two final electromagnetic 'jets', according to step (iii) of the process, are coplanar with the beam direction and have energies E_1, E_2 and scattering angles θ_1, θ_2 satisfying the transverse kinematical constraint

$$E_1 sin\theta_1 = -E_2 sin\theta_2 \tag{3.2}$$

but with

$$E_1 cos\theta_1 \neq -E_2 cos\theta_2. \tag{3.3}$$

As, in general, $E_1 \neq E_2$, one expects $\theta_2 \neq \pi - \theta_1$, i.e. the two particles are not back-to-back in the laboratory. The event corresponds to initial particles for step (ii) with energies

$$E_1^0 = E_1 cos^2\frac{\theta_1}{2} + E_2 sin^2\frac{\theta_2}{2} \tag{3.4}$$

$$E_2^0 = E_1 sin^2\frac{\theta_1}{2} + E_2 cos^2\frac{\theta_2}{2}. \tag{3.5}$$

E_1^0 and E_2^0 cannot be measured directly but must be inferred from E_1, E_2 through eqs. (3.4), (3.5). The probability for step (ii) to be started by particles of energy $E_i^0 = x_i E_b$, with $x_i < 1$, at a total energy squared $s_b = 4E_b^2$ can be described by a distribution $D(x_i, s_b)$, also known as the radiator, which is the same for the electron and the positron.

The observed cross section for a final electron scattered in the laboratory at an angle θ_1 for beam energy E_b can then be written, inclusively on the final electron energy, as

$$d\sigma_{obs}(E_b, \theta_1) = \int dx_1 \int dx_2 D(x_1, s_b) D(x_2, s_b) d\sigma_{lab}(E_1^0, E_2^0, \theta_1). \tag{3.6}$$

Kinematical cuts, such as, say, $E_1 > E_{min}$, are easily imposed by suitably restricting the integration regions of x_1 and x_2.

As mentioned above, in their cms the two particles have equal energies $E_1^* = E_2^* = E$ and scattering angles $\theta_1^* = \theta, \theta_2^* = \pi - \theta$. These are related to the corresponding quantities in the laboratory by

$$s = 4E_1^0 E_2^0 = 4E^2, \qquad E = \sqrt{E_1^0 E_2^0} \tag{3.7}$$

$$t = -2E_1^0 E_1(1 - cos\theta_1) = -2E^2(1 - cos\theta) \tag{3.8}$$

$$sin^2\frac{\theta}{2} = \frac{E_1^0}{E_1^0 sin^2\frac{\theta_1}{2} + E_2^0 cos^2\frac{\theta_1}{2}} sin^2\frac{\theta_1}{2}. \tag{3.9}$$

If $\overline{|B(s,t)|^2}$ is the square invariant amplitude relevant to Bhabha scattering and s, t are given by eqs. (3.10), (3.11), the differential cross sections in the center of mass and laboratory systems can be written as

$$d\sigma_{cms}(E, \theta) = \frac{1}{8E^2}\overline{|B(s,t)|^2}\frac{dcos\theta d\phi}{8(2\pi)^2}, \tag{3.10}$$

$$d\sigma_{lab}(E_1^0, E_2^0, \theta_1) = \frac{1}{8E_1^0 E_2^0}\overline{|B(s,t)|^2}\frac{E_1^0}{E_1^0 sin^2\frac{\theta_1}{2} + E_2^0 cos^2\frac{\theta_1}{2}}\frac{dcos\theta_1 d\phi}{8(2\pi)^2}. \tag{3.11}$$

In the following, we give the relevant formulae in the standard electroweak theory for eq. (3.13). They apply directly to the observed events only as far as the energy losses of step (i) are within the experimental energy resolution; otherwise one has to use eq. (3.14), for instance in the context of eq. (3.9). E and θ can be evaluated from E_1^0, E_2^0, θ_1 by means of eqs. (3.10), (3.12).

3.2 The lowest order cross section

We give here the formulae for Bhabha scattering lowest order differential cross section on the Z_0 resonance [15]. We take as independent parameters α, M_Z, the Fermi constant, $G_F = 1.16637(2) \cdot 10^{-5}\ GeV^{-2}$ and introduce $\overline{s}_w^2$ related to them through the relation

$$\overline{s}_w^2 \equiv \frac{1}{2}\left\{1-\left[1-\frac{4\mu^2}{\rho M_Z^2(1-\Delta\alpha)}\right]^{\frac{1}{2}}\right\}, \tag{3.12}$$

where

$$\mu \equiv \left(\frac{\pi\alpha}{\sqrt{2}G_F}\right)^{\frac{1}{2}} = 37.281\ GeV, \tag{3.13}$$

$\Delta\alpha \simeq 0.06$ is the vacuum polarization correction and

$$\rho = \frac{1}{1-\Delta\rho}, \qquad \Delta\rho = 3\frac{G_F m_t^2}{8\pi^2\sqrt{2}}, \tag{3.14}$$

m_t being the top mass; the following combinations will also be used

$$v_e = -1 + 4\overline{s}_w^2, \qquad \alpha_e = -1, \tag{3.15}$$

$$r_V = \frac{v_e^2}{v_e^2+\alpha_e^2}, \qquad r_A = \frac{\alpha_e^2}{v_e^2+\alpha_e^2}. \tag{3.16}$$

The coupling of the electron to the Z_0 occurs through the form factors

$$\chi(s) = \frac{\rho M_Z^2}{16\mu^2}(v_e^2+\alpha_e^2)\frac{s}{(s-M_Z^2+is\Gamma_Z/M_Z)}, \tag{3.17}$$

$$\chi'(t) = \frac{\rho M_Z^2}{16\mu^2}(v_e^2+\alpha_e^2)\frac{1}{2}\frac{s}{(M_Z^2-t)}, \tag{3.18}$$

where the s-dependent width $\Gamma_Z(s/M_Z^2)$, rather than Γ_Z, has been introduced.

If $s = 4E^2$ and $z = cos\theta$, E and θ being the energy and the scattering angle in the cms, the lowest order differential cross section, corresponding to the graphs of fig. 3.1, can be written as

$$\frac{d\sigma_0}{d\Omega} = \sum_{i=1}^{10}\frac{d\sigma_0^{(i)}}{d\Omega}, \tag{3.19}$$

where the different channels contributions are

$$d\sigma_0^{(1)}[\gamma(s),\gamma(s)] = \left(\frac{\alpha^2}{4s}\right)(1+z^2)d\Omega; \tag{3.20}$$

$$d\sigma_0^{(2)}[\gamma(s),\gamma(t)] = \left(\frac{\alpha^2}{4s}\right)\left[-\frac{2(1+z)^2}{(1-z)}\right]d\Omega; \tag{3.21}$$

$$d\sigma_0^{(3)}[\gamma(t),\gamma(t)] = \left(\frac{\alpha^2}{4s}\right)\frac{2}{(1-z)^2}[(1+z)^2+4]d\Omega; \tag{3.22}$$

$$d\sigma_0^{(4)}[\gamma(s),Z(t)] = \left(\frac{\alpha^2}{4s}\right)[-2\chi'(t)(1+z)^2]d\Omega; \tag{3.23}$$

$$d\sigma_0^{(5)}[\gamma(t),Z(t)] = \left(\frac{\alpha^2}{4s}\right)\frac{4\chi'(t)}{(1-z)}[(1+z)^2+4(r_V-r_A)]d\Omega; \tag{3.24}$$

$$d\sigma_0^{(6)}[Z(t),Z(t)] = \left(\frac{\alpha^2}{4s}\right)2[\chi'(t)]^2[(1+z)^2(1+4r_Vr_A)+4(1-4r_Vr_A)]d\Omega; \tag{3.25}$$

$$d\sigma_0^{(7)}[Z(s),\gamma(s)] = \left(\frac{\alpha^2}{4s}\right)2[Re\chi(s)][(1+z^2)r_V+2zr_A]d\Omega; \tag{3.26}$$

$$d\sigma_0^{(8)}[Z(s),\gamma(t)] = \left(\frac{\alpha^2}{4s}\right)\left[-2[Re\chi(s)]\frac{(1+z)^2}{(1-z)}\right]d\Omega; \tag{3.27}$$

$$d\sigma_0^{(9)}[Z(s),Z(t)] = \left(\frac{\alpha^2}{4s}\right)[-2[Re\chi(s)]\chi'(t)(1+z)^2(1+4r_Vr_A)]d\Omega; \tag{3.28}$$

$$d\sigma_0^{(10)}[Z(s),Z(s)] = \left(\frac{\alpha^2}{4s}\right)|\chi(s)|^2[(1+z^2)+8zr_Vr_A]d\Omega. \tag{3.29}$$

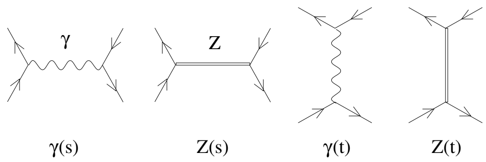

Figure 3.1: *Lowest order graphs for Bhabha scattering with their amplitudes .*

3.3 The radiative corrections

To set the terminology in a way useful to our description, we call electroweak radiative corrections the whole set of radiative corrections [15]. The one-loop corrections can then be subdivided into the following subclasses [15], [17]:

- QED corrections. They are further subdivided into
  - virtual corrections, which consist of those diagrams with an extra photon added to the Born graphs as a virtual photon loop (vertex and box diagrams). They also include the photon self energy (vacuum polarization) graphs [18]. They are depicted in fig. 3.2.
  - bremsstrahlung corrections, which consist of those diagrams with an extra photon added to the Born graphs as a real bremsstrahlung photon (fig. 3.3).
- Weak corrections, which collect all other one-loop diagrams: the subset of diagrams which involve corrections to the vector boson propagators γ, Z (fig. 3.4(a)), box diagrams with two massive boson exchange (fig. 3.4(b), (c)) and the set of vertex corrections (where the virtual photon contributions have been removed) (fig. 3.4(d), (e)). They contribute less than 1 % at most to wide angle Bhabha scattering and are negligible at small angles [20].

Due to the smallness of the electron mass the lowest order Higgs exchange diagram can be neglected. For the same reason also diagrams with Higgs - gauge boson mixing and box diagrams where one or both of the internal vector bosons of fig. 3.4 are replaced by Higgs scalars are negligible. The propagator corrections, however, involve all particles of the model, in particular the Higgs boson and the top quark, and thus depend on M_H and m_t. The vertex corrections of fig. 3.4 contain only W and Z in virtual states.

Theoretical calculations should include the complete electroweak lowest order contributions and first order radiative corrections with the Z_0 on resonance and at least most of the large higher order QED radiative corrections.

The differential cross section with first order virtual and real soft radiative corrections, including the vacuum polarization corrections, can be written as

$$\frac{d\sigma}{d\Omega} = \sum_{i=1}^{10}\frac{d\sigma_0^{(i)}}{d\Omega}(C_{infra}^{(i)} + C_F^{(i)}). \tag{3.30}$$

In the above formula, the coefficient which appears with brackets in the r.h.s. is somewhat arbitrarily split into a part C_{infra}, which depends on the soft cutoff

$$\Delta \equiv \frac{\Delta\omega}{E}, \tag{3.31}$$

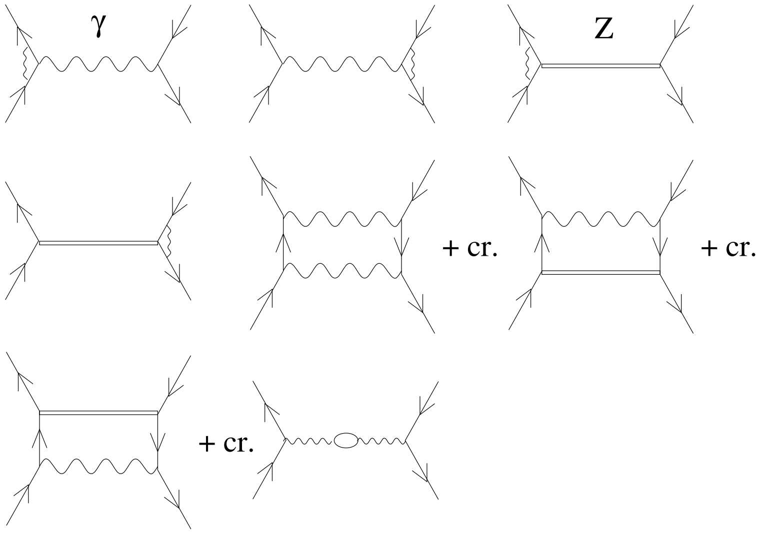

Figure 3.2: *Virtual graphs in the s channel .*

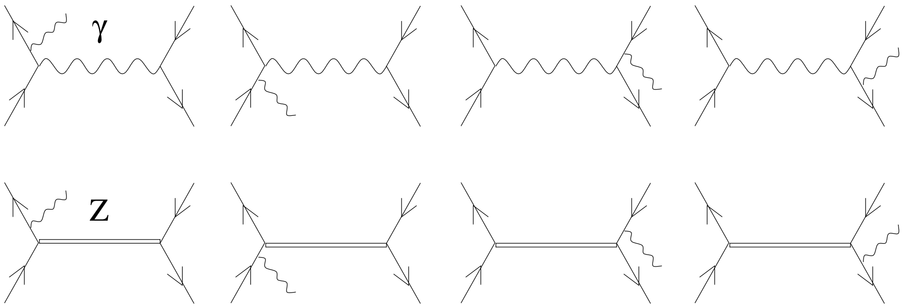

Figure 3.3: *Bremsstrahlung graphs in the s channel .*

the energy $\Delta\omega$ being the separation between the soft (undetected) and the hard (detected) radiation and a leftover part C_F. Analytical expressions for $C^{(i)}_{infra}$ and $C^{(i)}_F$ can be found in [15].

When including also the hard photons emitted collinearly to the final particles, inside a cone of half opening angle δ, one has

$$\frac{d\sigma}{d\Omega} = \sum_{i=1}^{10} \frac{d\sigma_0^{(i)}}{d\Omega}(\tilde{\mathrm{C}}^{(i)}_{infra} + \tilde{\mathrm{C}}^{(i)}_F). \tag{3.32}$$

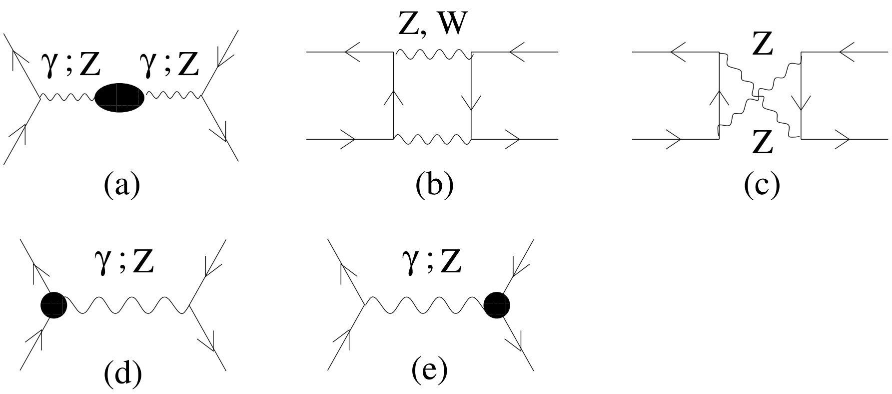

Figure 3.4: *Weak graphs in the s channel .*

At first order,

$$\tilde{C}^{(i)}_{infra} = C^{(i)}_{infra} + (\beta_\delta - \beta_e) ln\Delta \tag{3.33}$$

and

$$\tilde{C}^{(i)}_F = C^{(i)}_F + \frac{3}{4}(\beta_\delta - \beta_e) + \left(\frac{\alpha}{\pi}\right)\left(3 - \frac{2}{3}\pi^2\right) \tag{3.34}$$

where

$$\beta_\delta = 4\left(\frac{\alpha}{\pi}\right) ln\left(\frac{2}{\delta}\right), \tag{3.35}$$

$$\beta_e = 2\left(\frac{\alpha}{\pi}\right)\left[ln\left(\frac{s}{m_e^2}\right) - 1\right], \tag{3.36}$$

$$\delta = arctan\frac{(s\Delta + M_Z^2 - s)}{M_Z\Gamma_Z} - arctan\frac{(M_Z^2 - s)}{M_Z\Gamma_Z}. \tag{3.37}$$

The above formulae have been implemented in a numerical Fortran program, called bhabha.for, which can be found in the directory vxcern::disk$t3:[caffo.bhabha.bhanum] [16]. We will show distributions from the program in the next section.

3.4 Bhabha scattering at very small angles

For very small scattering angles, such as $5 < \theta < 50$ $mrad$, the process is dominated by the t-channel contributions (even on top of the Z_0 resonance) which have rather low exchanged 4-momentum ($\sqrt{-t} \approx 250 - 2500$ MeV). In this conditions pure QED describes very well the process, which is therefore well suited for luminosity monitoring. The lowest-order differential cross section in the high-energy limit is [19]

$$d\sigma_0^{QED} = \frac{\alpha^2}{16s}\left(\frac{3+z^2}{1-z}\right)^2 d\Omega. \tag{3.38}$$

where $z = cos\theta$. For very small scattering angles the differential cross section can be simplified to

$$d\sigma_0^{QED} = \frac{4\alpha^2}{s}\frac{1}{\theta^4}d\Omega \tag{3.39}$$

showing the large forward peak, which insures a low statistical error for the measurement.

In fig. 3.5, we plot[1] the differential cross section from eq. (3.22) and eq. (3.25). We see that the γ exchange in the t channel practically coincides with the total cross section. We give the minor, non vanishing term contributions in fig. 3.8 for comparison. In fig. 3.6, we show the integrated $t-\gamma$ cross section from 5 to 7 $mrad$ for the tree result (green curve) and for four corrections:

- correction 1: tree result plus first order (virtual and soft) QED radiative corrections (dark blue curve),
- correction 2: as correction 1, with exponentiation of soft photons (red curve),
- correction 3: as correction 1, plus first order final hard collinear photons (magenta curve),
- correction 4: as correction 3, with virtual, soft and hard corrections exponentiated [16] (light blue curve).

In fig. 3.7, we show the differential $t-\gamma$ cross section for the tree result and the four corrections above. All differential cross section plots have been calculated at cms energy 91.1 GeV.

The radiative corrections are sensitive only to the soft cutoff Δ; at $\sqrt{s} = M_Z = 91.1$ GeV, in the notation of eq. (3.25) one finds for instance $d\sigma_0^{(3)}/d\theta = 2.51 \cdot 10^5$ $nb, 3.92 \cdot 10^3$ nb at $\theta = 10, 40$ $mrad$; due

[1] The plots of figs. 3.5, 3.6, 3.7 and 3.8 have been produced by bhabha.for. The VSAT-modified version of the program together with all output files can be found in the vax directory WSDE99$DKB500:[VSAT.CHRISTINA.BHABHA].

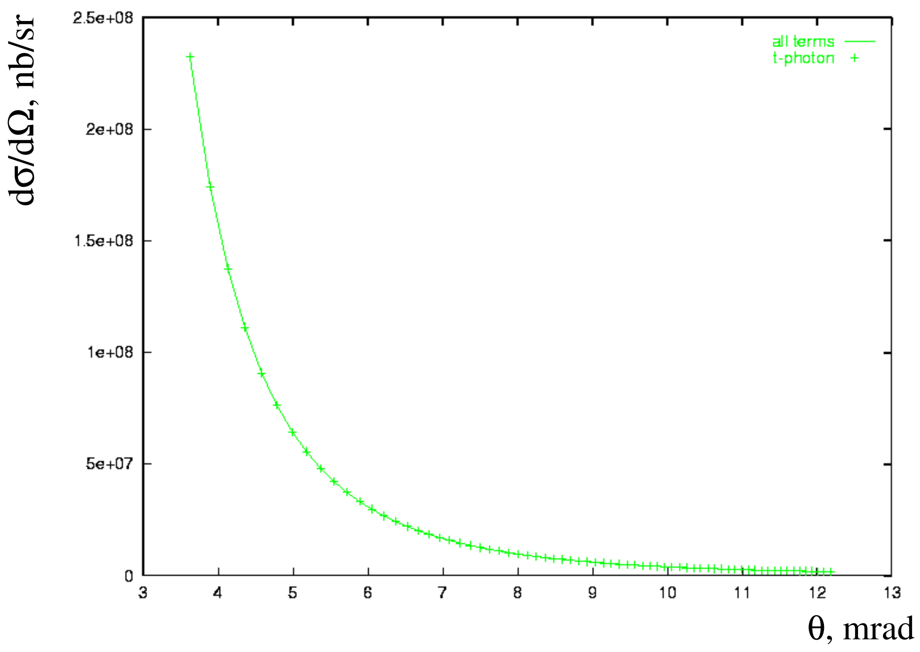

Figure 3.5: *Differential Bhabha cross section for all tree graphs and for $t-\gamma$ exchange .*

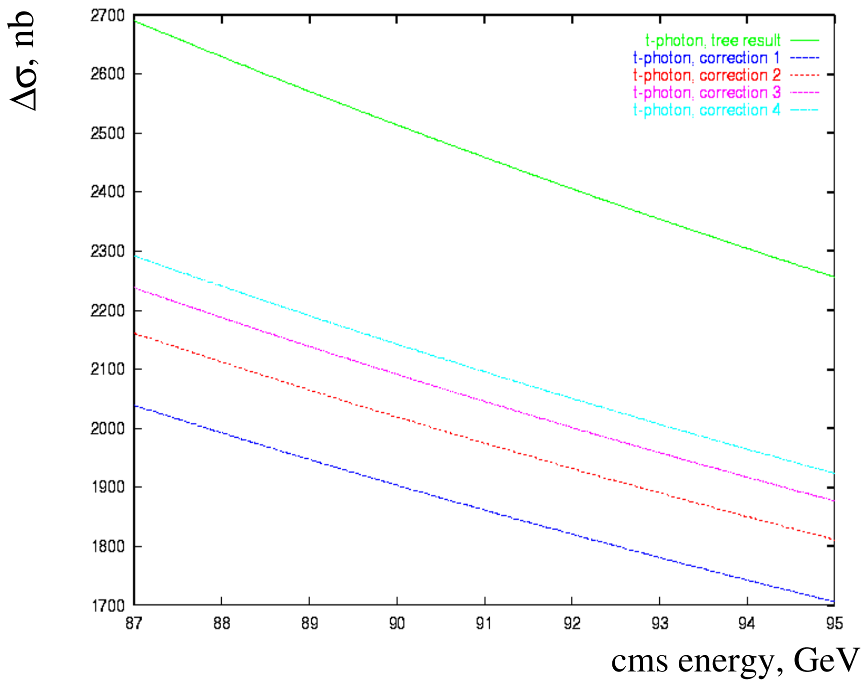

Figure 3.6: *Integrated $t-\gamma$ cross section, tree result and corrections .*

to radiative corrections, those values become $2.15 \cdot 10^5$ nb, $3.32 \cdot 10^3$ nb at $\Delta = 0.05$ and $2.26 \cdot 10^5$ nb, $3.54 \cdot 10^3$ nb at $\Delta = 0.10$.

As the scattering angle increases, the electroweak contributions become more important and at $\theta > 0.7$ rad, i.e. $\approx 40^0$, the dominant contribution is due to the s-channel Z_0 exchange. The process of this kinematical configuration is measured in the central electromagnetic calorimeter. After extraction of the less interesting t-channel part, it can give information on the line shape and on the $e - Z^0$ couplings (at variance with the $e^+e^- \to \mu^+\mu^-$ case, in Bhabha scattering there is a forward-backward asymmetry due to the interference between t and s channel amplitudes even in pure QED).

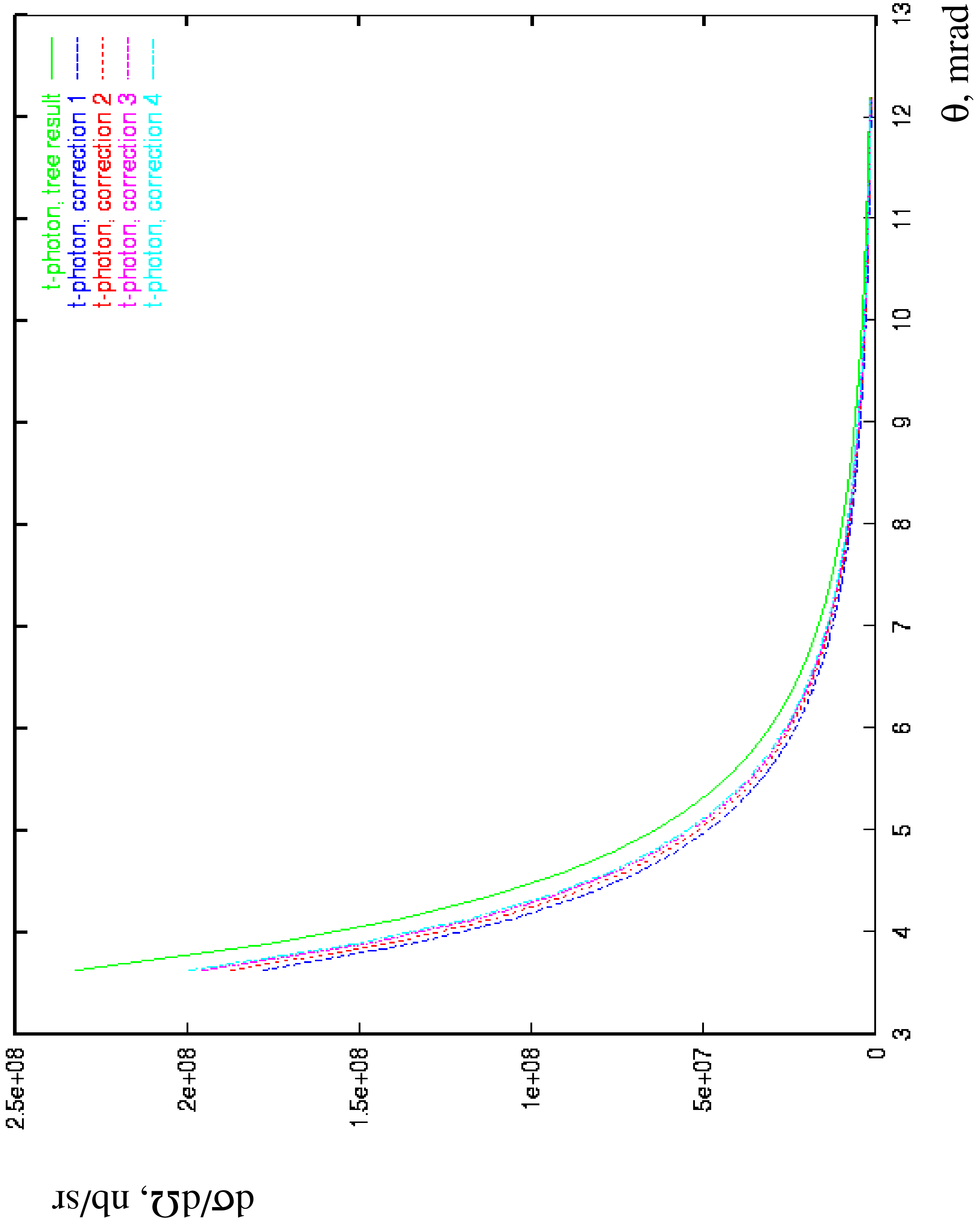

Figure 3.7: *Differential* $t-\gamma$ *cross section, tree result and corrections .*

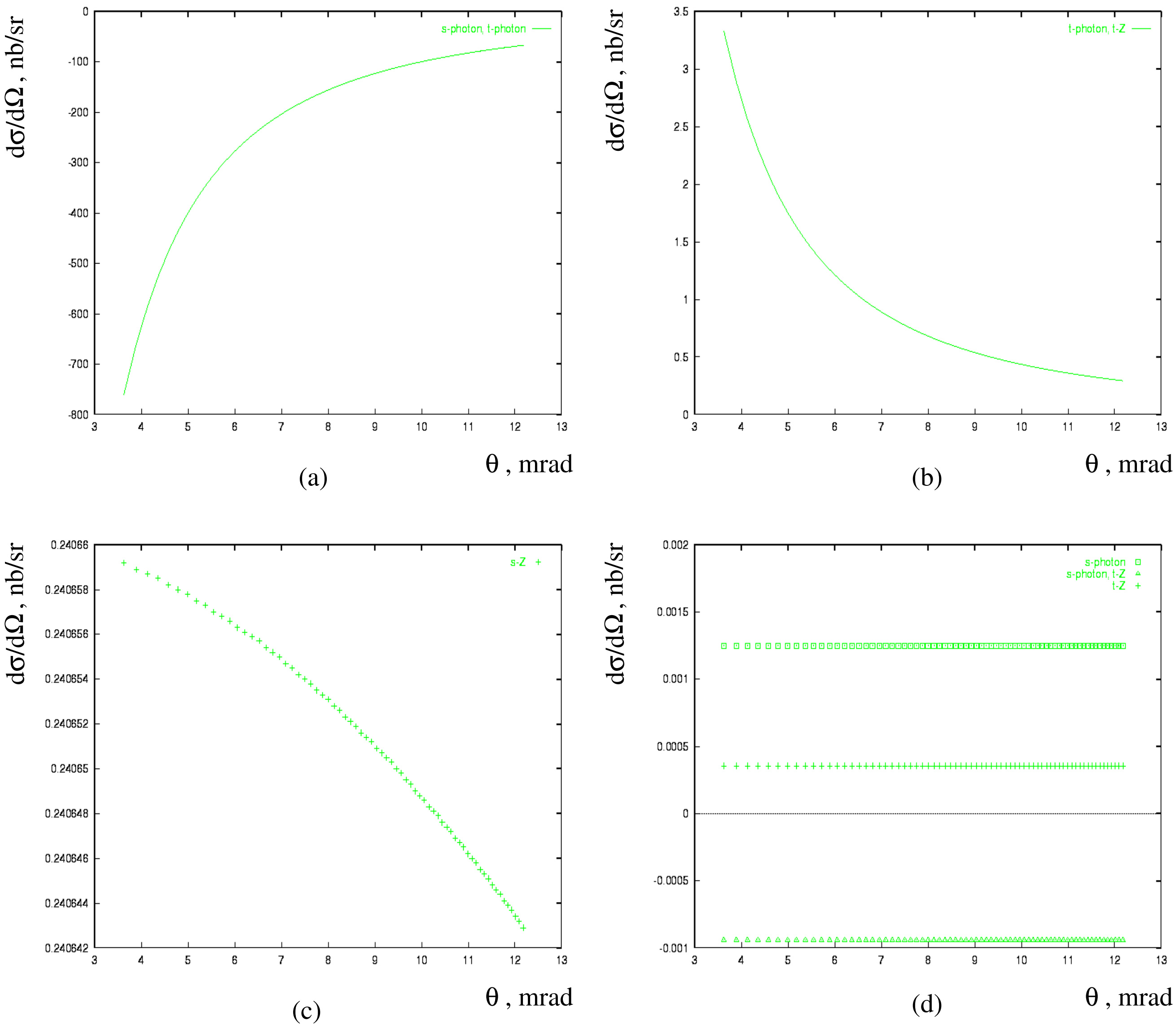

Figure 3.8: *Differential Bhabha cross section for (a)* $s-\gamma$, $t-\gamma$ *interference, (b)* $t-\gamma$, $t-Z$ *interference, (c)* $s-Z$ *exchange and (d)* $s-\gamma$ *exchange,* $s-\gamma$, $t-Z$ *interference and* $t-Z$ *exchange .*

Chapter 4

The Bhabha Measurement

In this chapter, we describe how our data are processed off-line in order to extract the Bhabha sample we need for the luminosity estimation. The procedure is the same for every year, but the additional features of the 95 scan data are also addressed here. The operation of the electronics is briefly explained as well, as its impact on the off-line analysis was of major importance.

4.1 The electronics

For the 1995 scan LEP had modified its previous mode of single bunch operation to a scheme of tightly spaced minibunch-trains, i.e. instead of having only one bunch crossing every 25 μs there were 2 to 4 minibunches within each bunch. The time separation between minibunches was a fraction of a μs. Most of the scan data taking was done with 3 minibunches separated by about 250 ns.

Each VSAT module was equipped with an independent system for reading pulse heights. This allowed for signals from different minibunches to be read in the four modules after the same beam crossing. Fig. 4.1 shows how the readout was done [21]. A fixed time (dt1) after a beam crossing (BCO), a signal from Pandora (WNG1) enables a gate generator. The width of each gate is about 50 ns. During this time a sensor is active and checks whether the sum of the FAD signals is above threshold. If this is the case, a HOLD is sent to the FADs when the gate is closed. A second HOLD is sent to the strips a fixed time later (dt2). If no signal is found above threshold during the gates, another signal from Pandora (WNG2) disables the gate generator after time dt3 and the HOLDs are generated. The minibunch number assigned to the signal is determined by the first gate during which the pulse is above threshold.

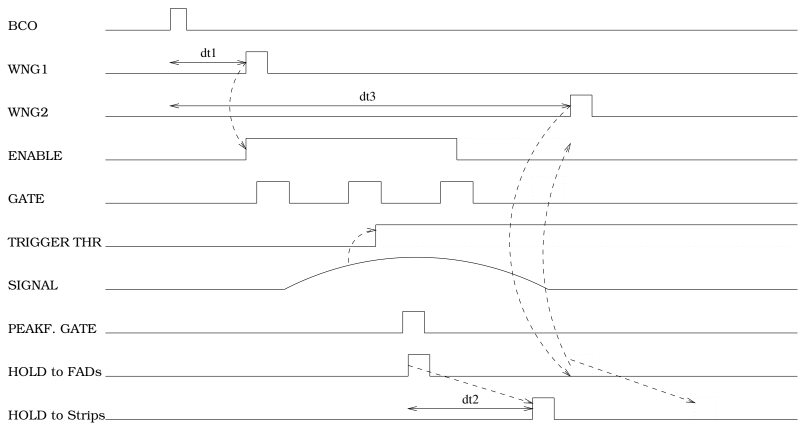

Figure 4.1: *Minibunch scheme signals when there is a hit in the module (full lines) and when there is no hit in the module (dotted lines).*

The independent operation of the modules occasionally resulted in misidentification of the minibunch number. This meant that elaborate off-line corrections had to be applied to the data both for the minibunch number recovering [22] and for the energy calibration [23].

4.2 The energy measurement

One example of mismatched event, i.e. wrong assignment of minibunch number by the electronics, is shown in fig. 4.2. The green pulse is a minibunch three electron. However, its energy is so high that the signal is already above threshold while gate G2 is open. This induces the detector to assign minibunch number two to the electron.

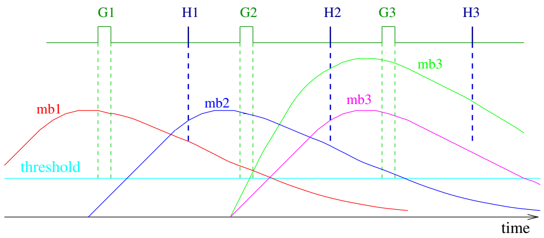

Figure 4.2: *Signals for the three minibunches and for one high energy mismatch.*

The subsequent hold H2 sees a value of the signal which is much higher than the one hold H3 would have seen. The result is that the electron, apart from having wrong minibunch number, it is also assigned an overestimated energy value. Those electrons form the green energy spectrum of fig. 4.3. The remaining minibunch three distribution (magenta curve) is manifestly missing many of its events if we compare its height with this of the minibunch one and two spectra (red and blue curves).

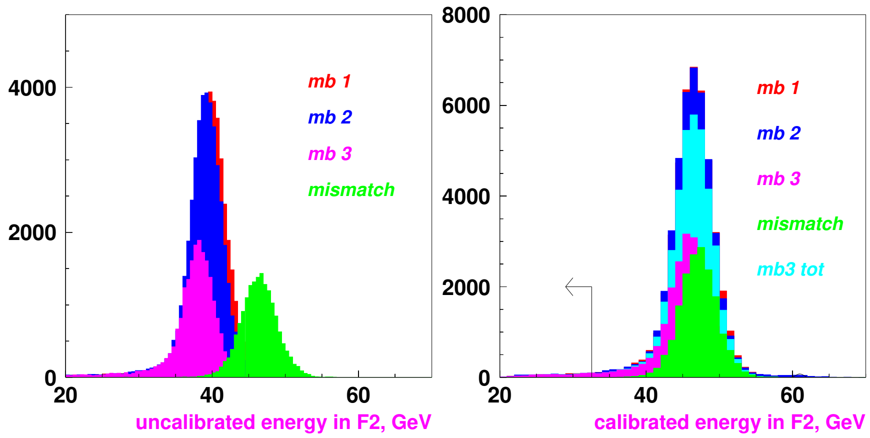

Figure 4.3: *Uncalibrated and calibrated energy distributions.*

In total, we had to deal with eight and six recoverable mismatching cases in diagonal one and two, respectively, the one above being the major one. The unrecoverable mismatches represent less than 0.1% of the data [22] and, therefore, can be safely neglected.

In spite of these complications, the energy calibration procedure confirmed the linearity of the modules. In fig. 4.4, we show the calibration constants for all four modules and three minibunches before and after the radiation accident [24]. We observe that they are sufficiently stable with beam energy.

After being calibrated, the Bhabha events have an energy cut applied on them, which removes particles that have less than 70% of the beam energy. These are mainly off-momentum electrons, representing few percent of the total sample. The cut is depicted by the black arrow in fig. 4.3. The next cut that we apply at this stage of the analysis is the cut on the showers having the maximum energy deposit in the outer x-strips of the detector as the shower may have started outside the module.

Bhabha events thus obtained have a very strong correlation in energy which can be seen in fig. 4.5 as the central aggregation of green points. This feature is considered to be their 'signature' and has played an important role in quality checking and also in the analysis (e.g. for recovering the mismatches). The plot includes also the off-momentum electrons and the radiative Bhabha events; they are the tails spreading over lower energies. The few events at very high energies are in reality pile-ups of off-momentum electrons

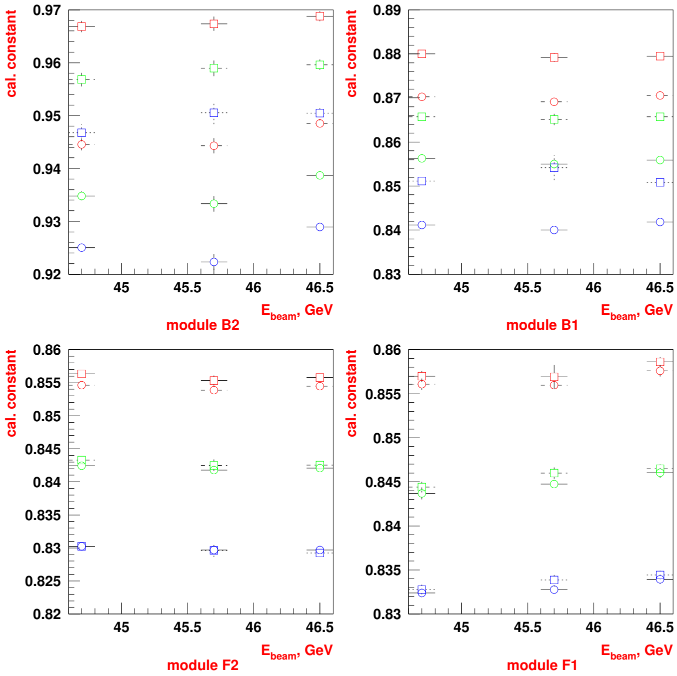

Figure 4.4: *Energy calibration constants for the four modules and minibunch one (red), minibunch two (green) and minibunch three (blue). The boxes (circles) show data before (after) the radiation accident.*

and Bhabha electrons. The reason why they are recorded as one event is that the detector did not have the time to disentangle them.

In order to complete this phase of the analysis we need to remove the accidental coincidences. They are shown as the blue circles of fig. 4.5. Their rate can be estimated and subtracted by tagging one particle in one module and one particle in the diagonal module separated in time by four beam crossings, i.e. after the same bunch has returned to the interaction point. They represent about 2% of the total background.

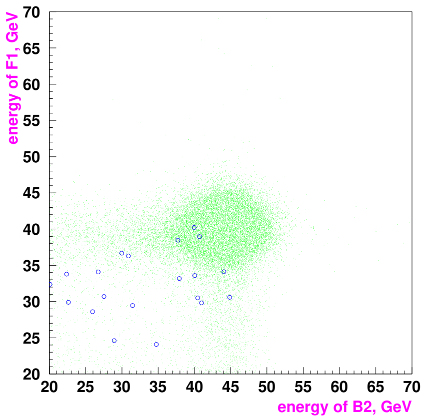

Figure 4.5: *Uncalibrated energy in diagonal 1 showing the Bhabha correlation (green blob) and the accidental Bhabha events (blue circles).*

4.3 The radial cut

After calibrating the energy and removing the background, the next step is to restrict the acceptance of the detector. This is done by the so-called radial cut, which defines a volume with outer edge corresponding to a maximum allowed radius of 7.7 cm (fig. 4.6(a)) and inner edge corresponding to a minimum allowed sum of the x positions ($sx = |x_{inner\ module}| + |x_{outer\ module}|$) equal to 13.2 cm (fig. 4.6(b)). The reason for the outer edge cut is the following [25]. Upstream of the VSAT modules (at about 6.5 m from the interaction point), the x radius of the beam pipe is increased from 6 cm to 8 cm. In the connection region there is a thick flange which strongly absorbs the electrons with a large angle. From the (x,y) distribution of the impact points of the electrons in the VSAT we see that the absorption is not sharp and also that it is difficult to reproduce it faithfully with the simulation. For this reason we set a cut at the value of the radius for which the (x,y) distributions of FASTSIM and of the data are compatible. A similar argument holds for the cut at the inner edge. Again, by comparing the sx distributions of simulation and data, we see that there are small differences (of the order of few permille) at small sx (there are too many Bhabha events in the simulation). The events with very small sx are those in which both the forward and the backward electron have a small angle and thus a small x, that is they are both close to the inner edge of the VSAT module. These events are difficult to simulate faithfully because they depend critically on many parameters (beam position, beam tilt, etc.) and thus we set an sx cut at the value for which the sx distributions of the simulation and of the data are compatible.

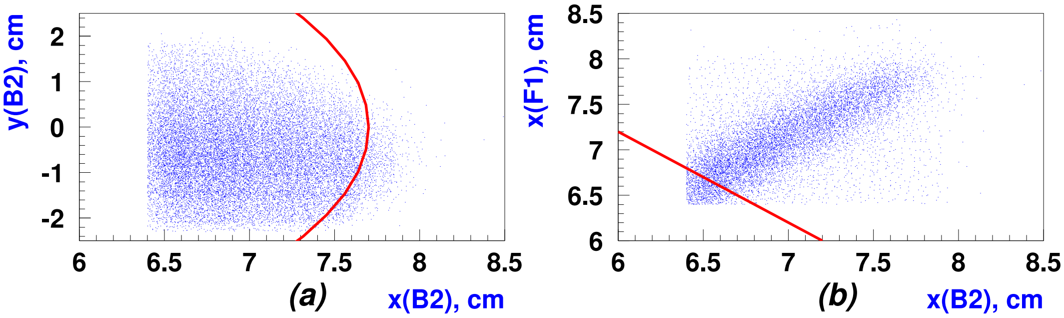

Figure 4.6: *The acceptance cuts; (a) the cut on the outer edge, (b) the cut on the inner edge of the detector.*

In fig. 4.7, we show the distributions of the number of Bhabha events per cassette for the fills of the scan. The mean value for the total volume (i.e. before applying the radial cut) is 3136 events per cassette in diagonal one and 3445 events per cassette in diagonal two. These numbers are reduced by 22% and 28%, respectively, when we apply our acceptance cut.

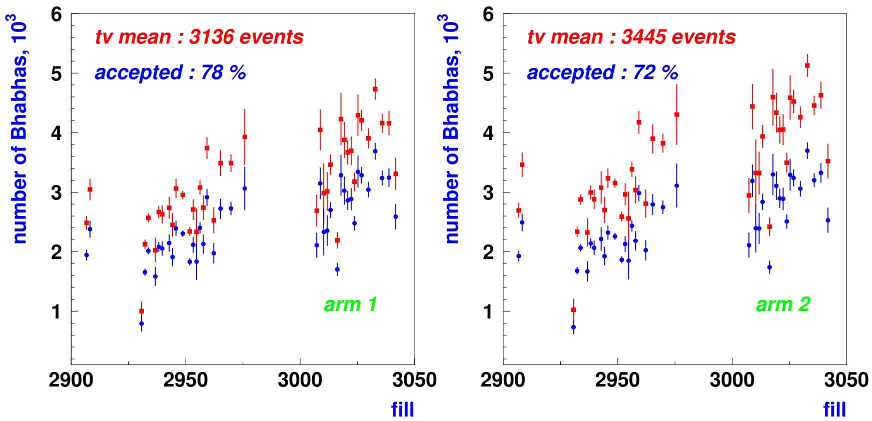

Figure 4.7: *Accepted events in the two diagonals before (red) and after (blue) the radial cut has been applied.*

4.4 Corrupted data

At this stage, we have a Bhabha sample consisting of 1200 cassettes. So far, our cuts have only restricted the number of events within each cassette, but all cassettes of the data taken have been included in the analysis. There are, however, cases where the cassettes are of bad quality and they have to be removed. In order to find out which cassettes are to be discarded we set two limits; first, the number of corrupted Bhabha triggers[1] must be less than 10% and second, the number of corrupted buffers must be less than 1 permille. The reason for applying this cut is that we correct for the corrupted events that we miss using the trigger information which is generally available even if the buffer is corrupted, but this is a correction which has a large uncertainty, so it is valid only if the fraction of corrupted data is small, otherwise it introduces an error larger than the gain in statistics we would have by including the corrupted cassettes [25].

Fig. 4.8 shows the distributions of these two variables and the positions of the cuts. In order to decide on the values of the cuts we try different combinations and we keep the one that gives us the largest number of cassettes possible without allowing the normalized differences between STIC and VSAT luminosities become too large. In total, the two cuts reject 31% of our cassettes.

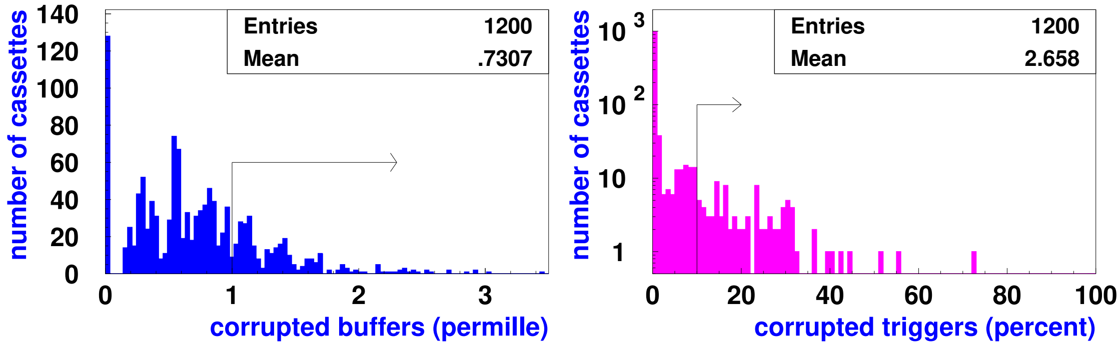

Figure 4.8: *Corrupted buffers and corrupted triggers for all scan data. The arrows show the position of the cuts.*

Fig. 4.9 shows the distributions of Bhabha events in the two diagonals (blue curves) for our final sample. The red curves show the cassettes that have been rejected because of the corrupted Bhabha trigger cut (only this cut would have removed 91 cassettes). The green curves show the cassettes that have been removed because of the corrupted buffer cut. This cut alone removes 307 cassettes. There were 25 cassettes that satisfied both cuts. We will continue the analysis of the remaining 827 cassettes in chapter 7.

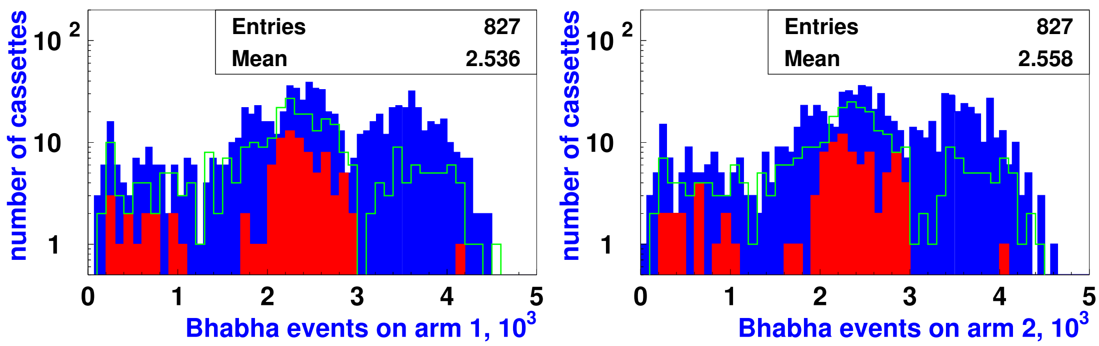

Figure 4.9: *The final Bhabha sample (blue curves). The red (green) distributions show cassettes with too many corrupted triggers (buffers).*

[1] A Bhabha trigger is a coincidence with more than 25 GeV deposited in each module.

Chapter 5

Beam Parameters

Due to the large accepted Bhabha cross section the VSAT can monitor with high statistics, besides the luminosity and the beam background, the variation of beam parameters as well. In this chapter, we give the results of the beam parameter analysis for the 1995 scan data as it is relevant for the luminosity calculation we will present in chapter 7. The results for 1993 and 1994 data can be found in [26] and [6]. A detailed description of the analysis is given in [27].

5.1 Why do we monitor beam parameters?

The monitoring of the beam parameters is an important task for two reasons.

The first reason is the online cross check of similar measurements done by the general monitoring system of LEP at the DELPHI interaction point. These measurements are used in order to optimize the luminosity, which depends strongly on the beam parameters. Among the DELPHI detectors, the VSAT has the highest accepted cross section and can thus collect sufficient statistics in a time interval ($\approx$ 10 minutes) relevant for online control.

The second reason is the offline estimation of variation of beam parameters. This information is used at different levels in the analysis of DELPHI events. For example, the variations of the beamspot position as well as those of the directions of the incident particles are used to optimize the alignment of the different DELPHI detectors. Furthermore, when it comes to the luminosity measurement done by the VSAT, the beam parameter monitoring provides an important cross check: the Bhabha cross section in the VSAT acceptance depends on the beam parameters and consequently, it has to be corrected for their variations. Fortunately, as shown in [28], such corrections can be done with a high level of accuracy (better than .1%) by using directly quantities measured by the VSAT without any need to know in detail the values of the beam parameters themselves. However, since the correction function is determined by an extensive simulation of different beam conditions done by a fast Monte Carlo program (FASTSIM), it is important to cross check the validity of the model used in FASTSIM by comparing the description of the variations of the beam parameters that we obtain from VSAT data with data from LEP or other DELPHI detectors.

5.2 Beam parameters monitoring with the VSAT

The beam parameters that are relevant for the following discussion are:

- the average values of the coordinates x_b, y_b and z_b of the interaction point;
- the corresponding beam widths σ_x, σ_y and σ_z;
- the average values of the incident positron and electron beam angles at the interaction point, in the (x, z) and in the (y, z) planes (we will call them briefly *tilts*), respectively θ^x_+, θ^x_-, θ^y_+ and θ^y_-;
- the beam divergence in the two planes, that is the spread around the above average angles.

The quantities measured with the VSAT which are used to extract information on the beam parameters are the x and y coordinates of the impact points of the scattered leptons in the four modules (fig. 5.1);

the angles of the outgoing particles cannot be measured, which disqualifies the detector for monitoring all the above mentioned parameters.

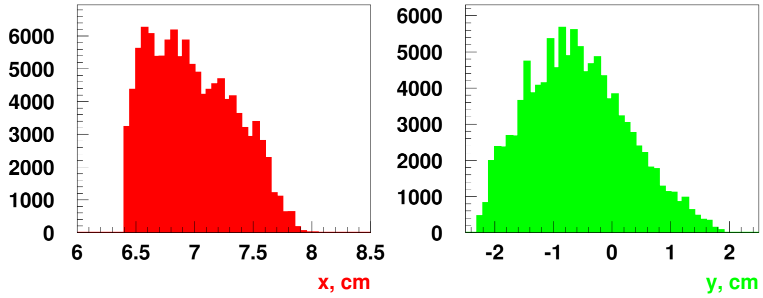

Figure 5.1: *x and y measurement for module F2, fill 3029.*

However, we can extract information on most of the beam parameters by combining the VSAT data with the beamspot measurements done by the VD and TPC. In this section, we will discuss the dependence on the beam parameters of the variables measured by the VSAT.

5.2.1 Beam parameters in the (x,z) plane

Figure 5.2 shows two Bhabha events in the (x,z) plane in the diagonals of the detector for the ideal situation in which the interaction point coincides with the nominal position ($x_b = y_b = z_b = 0$). We have assumed that the trajectories of the incoming particles are along the z-axis, so we also have zero beam tilts.

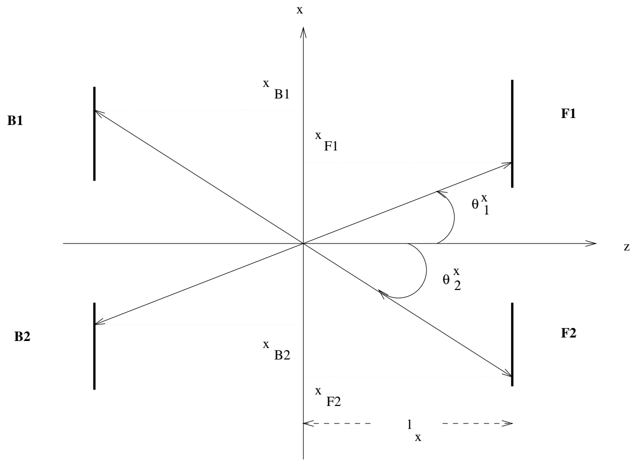

Figure 5.2: *Bhabha events on the two diagonals for zero beam displacement and zero tilts.*

In order to be able to represent the trajectories of the scattered particles as straight lines, we take into account the divergent effect of the superconducting quadrupoles (in first approximation) by moving the modules to an effective distance, l_x=12.6 m, which is assumed to be the same for all modules. The production angle of the Bhabha pair in diagonal i is denoted by θ_i^x and is defined to be always positive. Since those angles are very small we can calculate the x coordinates of the impact points of the particles on the modules as follows:

$$
\begin{aligned}
x_{F1} &= l_x \theta_1^x \qquad & x_{B2} &= -l_x \theta_1^x \\
x_{B1} &= l_x \theta_2^x \qquad & x_{F2} &= -l_x \theta_2^x
\end{aligned}
\tag{5.1}
$$

However, this ideal condition is rarely the case, since the beams do not usually cross at the nominal position. Fig. 5.3 represents a more realistic situation, in which we have included a nonzero beam displacement in the x direction, x_b. The constant f_x is the amplification factor of the particle trajectories due to the superconducting quadrupoles. It is of the order of 2.1 and it is practically the same for all four modules.

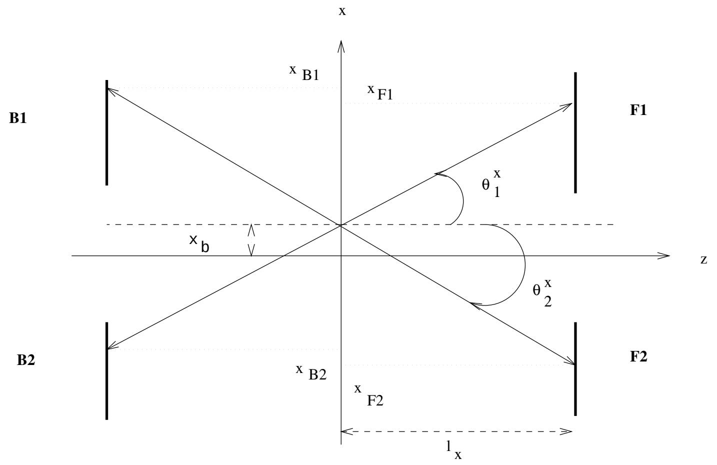

Figure 5.3: *Events on the two diagonals for zero z displacement and zero tilts.*

The emission angles are the same as in fig. 5.2, but the x coordinates of the impact points are now given by

$$
\begin{aligned}
x_{F1} &= f_x x_b + l_x \theta_1^x \qquad & x_{B2} &= f_x x_b - l_x \theta_1^x \\
x_{B1} &= f_x x_b + l_x \theta_2^x \qquad & x_{F2} &= f_x x_b - l_x \theta_2^x
\end{aligned}
\tag{5.2}
$$

The next step is to see how the impact points will be affected by a beam displacement in the z direction. We will therefore include a shift of the interaction point equal to z_b, as shown in fig. 5.4.

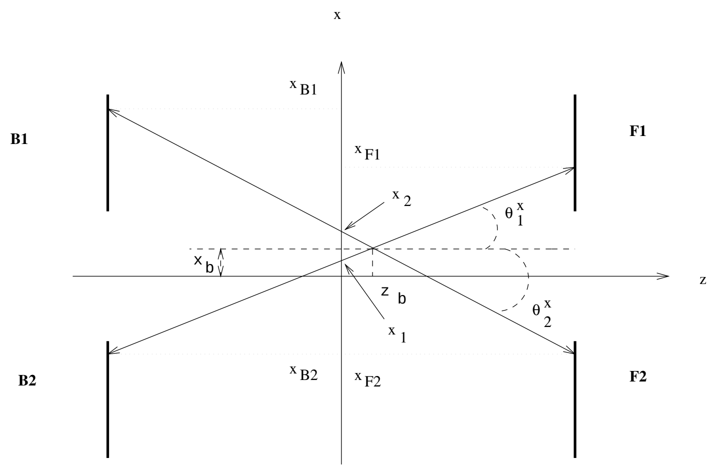

Figure 5.4: *Events on the two diagonals for nonzero beam displacements, x_b and z_b, and zero tilts.*

As evident from fig. 5.4, the effect of the z displacement is equivalent to that of two different x displacements, x_1 and x_2, in the two diagonals taken at z=0:

$$x_1 = x_b - z_b \theta_1^x \qquad x_2 = x_b + z_b \theta_2^x . \tag{5.3}$$

The impact points are thus given by

$$x_{F1} = f_x (x_b - z_b \theta_1^x) + l_x \theta_1^x \qquad x_{B2} = f_x (x_b - z_b \theta_1^x) - l_x \theta_1^x$$

$$x_{B1} = f_x(x_b + z_b\theta_2^x) + l_x\theta_2^x \qquad\qquad x_{F2} = f_x(x_b + z_b\theta_2^x) - l_x\theta_2^x. \tag{5.4}$$

We can now consider the case of nonzero tilts. Fig. 5.5 shows events in the two diagonals, where it has been assumed that the positron beam has a positive tilt, θ_+^x, whereas the electron beam has a negative tilt, θ_-^x. The equations for the x impact points will now be affected in terms of the production angle, namely

$$\begin{aligned} x_{F1} &= f_x x_b + l_x(\theta_1^x - |\theta_-^x|) = f_x x_b + l_x(\theta_1^x + \theta_-^x) \qquad x_{B2} = f_x x_b - l_x(\theta_1^x + |\theta_+^x|) = f_x x_b - l_x(\theta_1^x + \theta_+^x) \\ x_{B1} &= f_x x_b + l_x(\theta_2^x - |\theta_+^x|) = f_x x_b + l_x(\theta_2^x - \theta_+^x) \qquad x_{F2} = f_x x_b - l_x(\theta_2^x + |\theta_-^x|) = f_x x_b - l_x(\theta_2^x - \theta_-^x) \end{aligned} \tag{5.5}$$

If we combine eqs. (5.4) and (5.5), we obtain for the general case of nonzero beam displacements and nonzero tilts:

$$\begin{aligned} x_{F1} &= f_x(x_b - z_b(\theta_1^x + \theta_-^x)) + l_x(\theta_1^x + \theta_-^x) \qquad x_{B2} = f_x(x_b - z_b(\theta_1^x + \theta_+^x)) - l_x(\theta_1^x + \theta_+^x) \\ x_{B1} &= f_x(x_b + z_b(\theta_2^x - \theta_+^x)) + l_x(\theta_2^x - \theta_+^x) \qquad x_{F2} = f_x(x_b + z_b(\theta_2^x - \theta_-^x)) - l_x(\theta_2^x - \theta_-^x) \end{aligned} \tag{5.6}$$

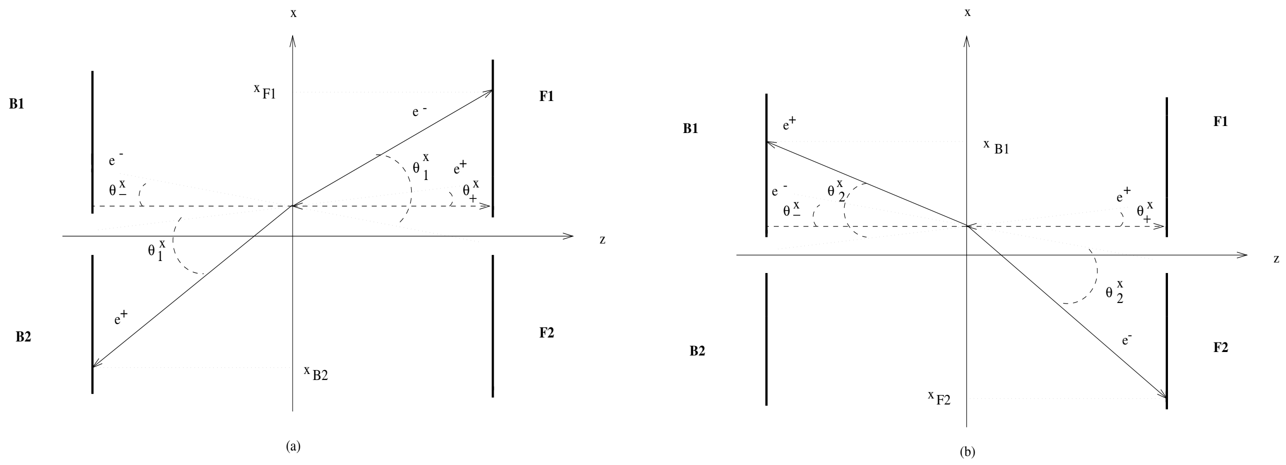

Figure 5.5: *Events for zero z displacement and nonzero tilts (a) on diagonal 1 and (b) on diagonal 2.*

From these equations, we see that it is convenient to define the following quantities:

$$\begin{aligned} \Delta x_1 &= x_{F1} + x_{B2} = 2\cdot f_x(x_b - z_b(\theta_1^x + \theta_x)) + \epsilon_x l_x \\ \Delta x_2 &= x_{F2} + x_{B1} = 2\cdot f_x(x_b + z_b(\theta_2^x - \theta_x)) + \epsilon_x l_x \end{aligned} \tag{5.7}$$

where we have defined the average tilt, θ_x, and the acollinearity, ϵ_x, as follows

$$\theta_x = \frac{\theta_+^x + \theta_-^x}{2} \qquad\qquad \epsilon_x = \theta_-^x - \theta_+^x \tag{5.8}$$

To better separate the dependence on different beam parameters, we define the following quantities:

$$\Delta x_0 = \frac{\Delta x_1 + \Delta x_2}{2} = 2\cdot f_x x_b + \epsilon_x l_x + f_x z_b(\theta_2^x - \theta_1^x - 2\theta_x) \tag{5.9}$$

$$\delta x = \Delta x_2 - \Delta x_1 = 2\cdot f_x z_b(\theta_1^x + \theta_2^x) \tag{5.10}$$

By taking the average over a reasonably long period of time (for this analysis, it is useful to use the time needed to write a cassette, which is about 20 minutes and corresponds to about 3000 events), we can substitute θ_1^x and θ_2^x with their average values, which are both very close to 5.5 mrad. This shows that δx essentially depends only on the value of z_b. On the contrary, Δx_0 essentially measures the combined effect of the beam x displacement and beam acollinearity in the (x,z) plane, since the third term in eq. (5.9) is completely negligible.

The similarity of the x_b and ϵ_x effects on the impact points is clearly depicted in fig. 5.6, where we have assumed for simplicity that only the electron beam has a nonzero tilt: the full lines correspond to outgoing particle tracks for $x_b = \theta_-^x = \theta_+^x = 0$, whereas the dotted line shows the case of nonzero acollinearity and x_b=0 and the dashed line shows an event with zero acollinearity but nonzero x_b, which has the same impact points on the modules, showing that the ϵ_x and x_b effects are equivalent, and therefore these two parameters cannot be determined separately using the VSAT information alone.

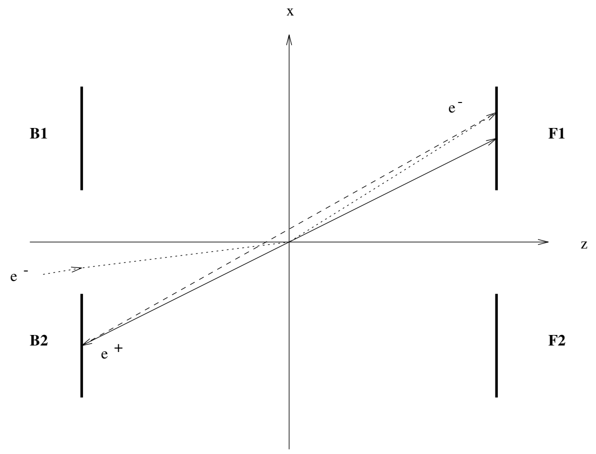

Figure 5.6: *Effects of the acollinearity and the x displacement on the impact points.*

There are two other useful measures that can be done with the VSAT and which are related to the beam tilt and production angles. With a view to this, it is helpful to consider events with equal (positive) beam tilt angles, θ_+^x and θ_-^x, as in fig. 5.7. The figure shows clearly that the (average) production angle on

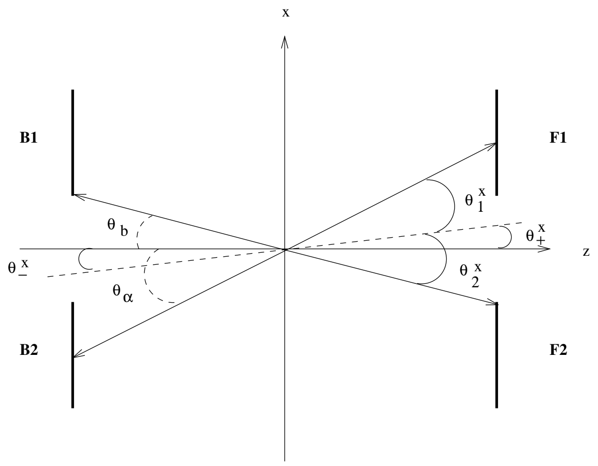

Figure 5.7: *Effect of the beam tilts on the production angles on the two diagonals.*

diagonal 1, θ_1^x, is smaller than in the case of zero tilts, where it would be equal to θ_α. The opposite holds for the production angle on diagonal 2: θ_2^x is larger than θ_b. Due to the rapid decrease of the Bhabha cross section with the angle, this induces an opposite variation of the number of accepted Bhabha events on the two diagonals: the number of events on diagonal 1, N_1, will increase, whereas the number of events on diagonal 2, N_2, will decrease. Therefore, we expect to observe a variation of the variable:

$$A_D = \frac{N_1 - N_2}{N_1 + N_2} \tag{5.11}$$

called diagonal asymmetry. It must be noted, however, that the diagonal asymmetry is only affected by the average tilt angle, θ_x, and not by the separate values of θ^x_- and θ^x_+. By consequence, it cannot be used to extract information on the acollinearity, ϵ_x. The relationship between A_D and θ_x has been determined by FASTSIM [25].

Finally, from eq. (5.9), we see that the average value $R\Delta x_0$ of the combined widths $R\Delta x_1$ and $R\Delta x_2$ of the Δx_1 and Δx_2 distributions is related to the widths σ_x and σ_z of the incident beams at the interaction point and to their divergences in the (x,z) plane.

5.2.2 Beam parameters in the (y,z) plane

The situation in this plane is analogous to what we saw in the previous section for the (x,z) plane, the only difference being that the superconducting quadrupoles have a convergent rather than a divergent effect. This induces a focusing of the scattered particle trajectories in the y direction, which in turn causes the detector to lose sensitivity.

We will repeat the calculations of section 5.2.1 briefly. First, we consider the simple case of no beam displacement and zero tilts (fig. 5.8). The modules have been moved to

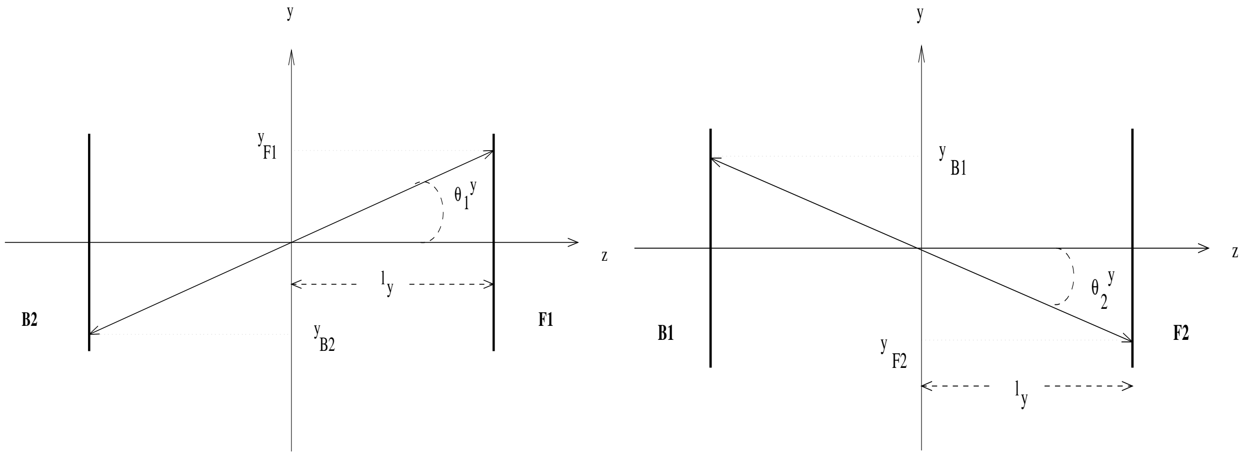

Figure 5.8: *Events on diagonals 1 and 2 for zero beam displacement and zero tilts.*

an effective distance, $l_y = 3.5$ m, due to the convergent effect of the quadrupoles. The same assumptions as in the case of the (x,z) plane apply here as well, i.e. l_y is the same for all modules and the production angles on the two diagonals, θ^y_1 and θ^y_2, are defined to be positive. The y coordinates of the impact points of the outgoing particles on the four modules are then given by

$$y_{F1} = l_y\theta^y_1 \qquad y_{B2} = -l_y\theta^y_1 \qquad y_{B1} = l_y\theta^y_2 \qquad y_{F2} = -l_y\theta^y_2 \tag{5.12}$$

The next step is to include a beam displacement in y, y_b. The factor f_y is of the order of 0.1. From fig. 5.9 we can calculate the y coordinates:

$$\begin{aligned} y_{F1} &= f_y y_b + l_y\theta^y_1 \qquad & y_{B2} &= f_y y_b - l_y\theta^y_1 \\ y_{B1} &= f_y y_b + l_y\theta^y_2 \qquad & y_{F2} &= f_y y_b - l_y\theta^y_2 \end{aligned} \tag{5.13}$$

We define

$$\Delta y_1 = y_{F1} + y_{B2} \qquad \Delta y_2 = y_{F2} + y_{B1} \tag{5.14}$$

The effect of a shift of y_b on those variables is similar to that of a shift of x_b on the corresponding quantities of the (x,z) plane: from the last equations we have $\Delta y_1 = \Delta y_2 = 2f_y y_b$, therefore the variables Δy_1, Δy_2 and $\Delta y_0 = (\Delta y_1 + \Delta y_2)/2$ vary proportionally to y_b, whereas the difference $\Delta y_1 - \Delta y_2$ is always zero. We can now continue to consider the situation presented in fig. 5.10, where we have assumed a positive z displacement, z_b. From the figure, we obtain

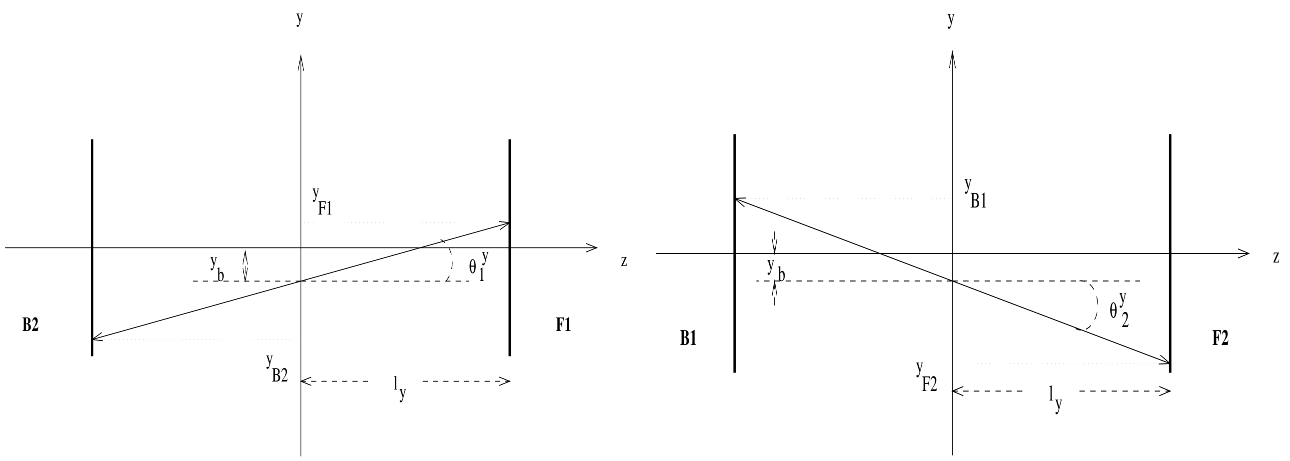

Figure 5.9: *Events on the two diagonals for zero z displacement and zero tilts.*

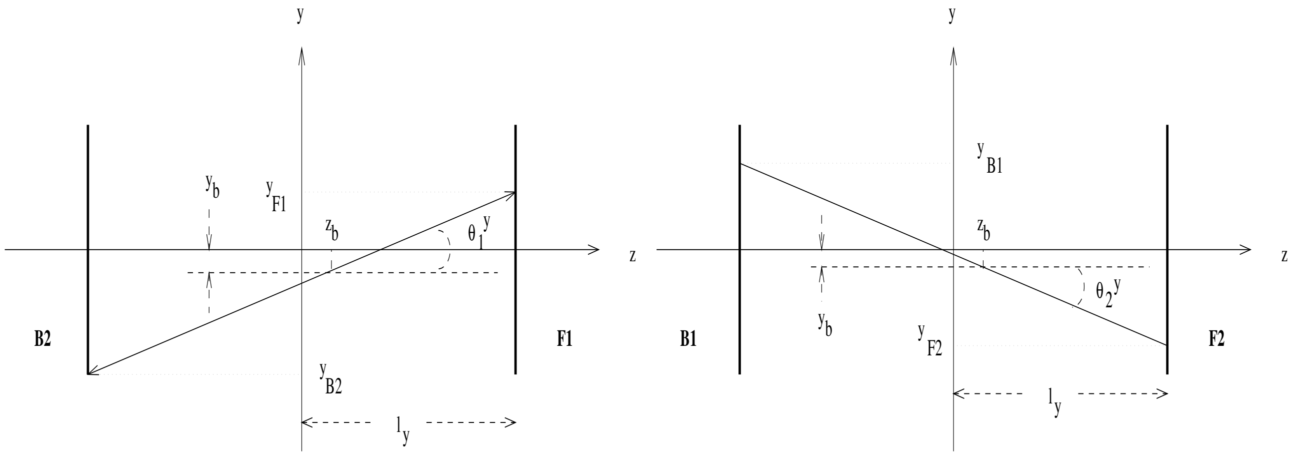

Figure 5.10: *Events on the two diagonals for nonzero z displacement and zero tilts.*

$$
\begin{aligned}
y_{F1} &= f_y(y_b - z_b\theta_1^y) + l_y\theta_1^y \qquad & y_{B2} &= f_y(y_b - z_b\theta_1^y) - l_y\theta_1^y \\
y_{B1} &= f_y(y_b + z_b\theta_2^y) + l_y\theta_2^y \qquad & y_{F2} &= f_y(y_b + z_b\theta_2^y) - l_y\theta_2^y
\end{aligned}
\tag{5.15}
$$

Consequently, the corrected factor is the one including the y_b value, which needs to have subtracted from (diagonal 1) or added to (diagonal 2) a quantity proportionally related to z_b. This induces a proportional variation of Δy_1 and Δy_2 with respect to z_b, now being given by

$$
\Delta y_1 = 2f_y(y_b - z_b\theta_1^y) \qquad \Delta y_2 = 2f_y(y_b + z_b\theta_2^y) \tag{5.16}
$$

again including both y_b and z_b in the same equation.

Lastly, the case of nonzero beam tilts has to be mentioned. The y displacement is again taken to be negative while the interaction point is assumed to have no displacement in the z direction. The positron (electron) beam has a positive (negative) tilt denoted by θ_+^y (θ_-^y). The situation is shown in fig. 5.11, from which it can be derived that

$$
\begin{aligned}
y_{F1} &= f_y y_b + l_y(\theta_1^y - |\theta_-^y|) = f_y y_b + l_y(\theta_1^y + \theta_-^y) \\
y_{B2} &= f_y y_b - l_y(\theta_1^y + |\theta_+^y|) = f_y y_b - l_y(\theta_1^y + \theta_+^y)
\end{aligned}
\tag{5.17}
$$

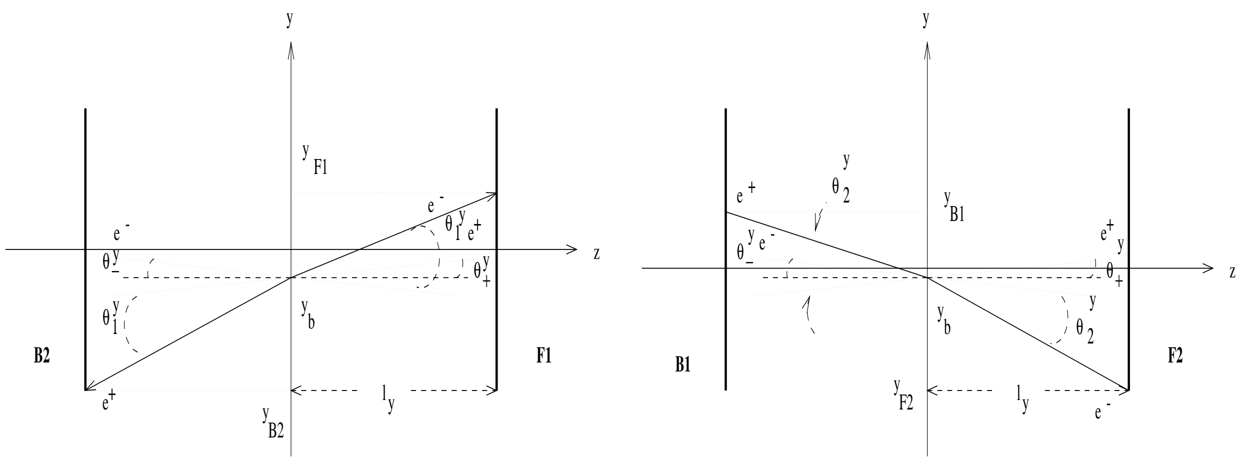

Figure 5.11: *Events on the two diagonals for zero z displacement and nonzero tilts.*

$$y_{B1} = -|f_y y_b| + l_y(\theta_2^y - |\theta_+^y|) = f_y y_b + l_y(\theta_2^y - \theta_+^y)$$
$$y_{F2} = f_y y_b - l_y(\theta_2^y + |\theta_-^y|) = f_y y_b - l_y(\theta_2^y - \theta_-^y)$$

The acollinearity in the (y,z) plane, $\epsilon_y = \theta_-^y - \theta_+^y$, affects the y coordinates of the impact points in the same way as y_b does, as can be seen in the following equation:

$$\Delta y_1 = \Delta y_2 = 2 f_y y_b + l_y(\theta_-^y - \theta_+^y) \tag{5.18}$$

By combining our conclusions so far, we can derive the equations for the case of both nonzero y and z displacement and nonzero tilts:

$$\begin{aligned} y_{F1} &= f_y(y_b - z_b(\theta_1^y + \theta_-^y)) + l_y(\theta_1^y + \theta_-^y) \qquad & y_{B2} &= f_y(y_b - z_b(\theta_1^y + \theta_+^y)) - l_y(\theta_1^y + \theta_+^y) \\ y_{B1} &= f_y(y_b + z_b(\theta_2^y - \theta_+^y)) + l_y(\theta_2^y - \theta_+^y) \qquad & y_{F2} &= f_y(y_b + z_b(\theta_2^y - \theta_-^y)) - l_y(\theta_2^y - \theta_-^y) \end{aligned} \tag{5.19}$$

from which

$$\Delta y_1 = 2 f_y(y_b - z_b(\theta_1^y + \theta_y)) + l_y \epsilon_y \qquad \Delta y_2 = 2 f_y(y_b + z_b(\theta_2^y - \theta_y)) + l_y \epsilon_y \tag{5.20}$$

Using the average values of Δy_1 and Δy_2 over one cassette we conclude that

$$\Delta y_0 = 2 f_y y_b + l_y \epsilon_y - f_y z_b(\theta_1^y - \theta_2^y + 2\theta_y) \tag{5.21}$$

The average values of θ_1^y and θ_2^y are very close to zero and also the product $f_y z_b \theta_y$ is extremely small, so the third term in the r.h.s. of eq. (5.21) is completely negligible.

One can also define the difference δy:

$$\delta y = \Delta y_2 - \Delta y_1 = 2 \cdot f_y z_b(\theta_1^y + \theta_2^y) \tag{5.22}$$

but, due to the very small values of f_y, θ_1^y and θ_2^y, δy is practically zero and thus carries no useful information on z_b.

5.3 Determination of the beamspot

From VSAT data alone we can estimate the z coordinate of the interaction point using eq. (5.10), but this is not possible neither for the x nor for the y coordinate. This is due to the fact that, as shown in eq. (5.9) and (5.21), the detector variables depend both on the beam displacement and on the acollinearity in those directions. However, we can use the beamspot values for x and y as they are determined by VD and TPC to obtain information on the variations of the acollinearity.

5.3.1 Estimation of the x beamspot

The evolution of Δx during the 1995 scan data taking is shown in fig. 5.12 (we recall that Δx represents the average value over the events of a cassette). Due to the limited VSAT acceptance in the x direction, this average value must be corrected, since Δx_1 and Δx_2 represent average values of rather broad distributions, which are affected in non trivial ways by different beam parameters, such as beam width, divergence and acollinearity.

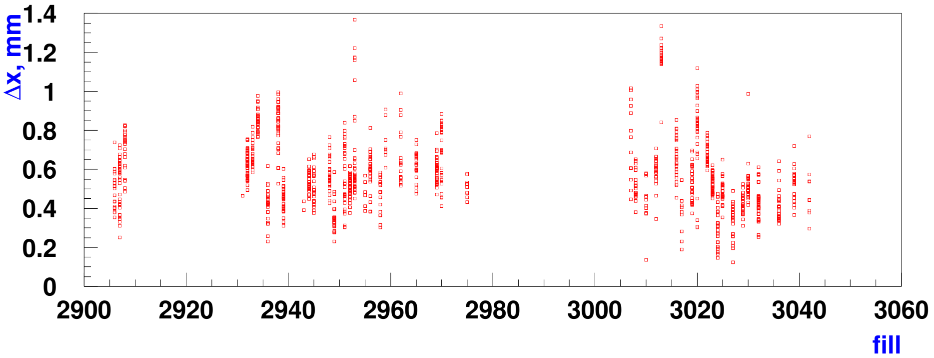

Figure 5.12: *Variations of Δx during the 1995 scan.*

Furthermore, the averaging procedure introduces a dependence of Δx_1 and Δx_2 on the y tilt. FASTSIM has shown that these effects can be parametrized in terms of quantities directly measured by the VSAT. The correction for the beam width and divergence effect can be expressed as a dependence on the widths of the Δx_1 and Δx_2 distributions, $R\Delta x_1$ and $R\Delta x_2$, respectively; the correction for the tilt in y can be achieved through the Δy_1 and Δy_1 distributions. The resulting relations are then [25]

$$\begin{aligned} \Delta x_{1C} &= \Delta x_1(1 + 0.1(R\Delta x_1 - 2.6)) - 0.1(\Delta y_1 + 7) \\ \Delta x_{2C} &= \Delta x_2(1 + 0.1(R\Delta x_2 - 2.8)) - 0.05(\Delta y_2 + 8) \end{aligned} \tag{5.23}$$

where all quantities are measured in mm. Consequently, Δx_0 and δx of eqs. (5.9) and (5.10) should be replaced by the quantities $\Delta x_C = (\Delta x_{1C} + \Delta x_{2C})/2$ and $\delta x_C = \Delta x_{2C} - \Delta x_{1C}$, respectively. It is convenient to define the quantity x_{VSAT} as follows:

$$x_{VSAT} = \frac{\Delta x_C}{2f_x} \tag{5.24}$$

It is then clear that, from eqs. (5.9) and (5.24),

$$x_{VSAT} = x_b + \epsilon_x \frac{l_x}{2f_x} + x_0 \tag{5.25}$$

where we have included in the offset x_0 the small term $\frac{z_b}{2}(\theta_2^x - \theta_1^x - 2\theta_x)$ of eq. (5.9), which is practically constant, since θ_1^x and θ_2^x are practically equal and θ_x is very small.

As evident from eq. (5.25), x_{VSAT} is directly related to x_b at fixed acollinearity. The distributions of x_{VSAT} for the scan and for the periods before and after the radiation accident (i.e. for fill < 3000 and for fill > 3000, respectively) are shown in fig. 5.13. The variation with fill number is shown in the same figure. The mean value for the entire scan was (0.162 ± 0.055) *mm*. The corresponding values before and after the accident were (0.168 ± 0.048) *mm* and (0.154 ± 0.062) *mm*, respectively. In fig. 5.14(a), x_{VSAT} is plotted versus x_{VD}. The figure shows a qualitative agreement and suggests a linear relation between the two measurements within an overall shift of the order of 3 mm.

In fig. 5.14(b), we have plotted the normalized difference to the expected errors in x_{VSAT} and x_{VD} measurements. This difference is given by the relation

$$\delta x_{norm} = \frac{x_{VSAT} - < x_{VSAT} > -(x_{VD} - < x_{VD} >)}{\sqrt{\sigma^2_{x_{VSAT}} + \sigma^2_{x_{VD}}}} \tag{5.26}$$

We see that the average fluctuation is about twice the expected value. Since the estimation of x_{VSAT} has been done under the assumption of fixed acollinearity, we conclude that the variations of this parameter

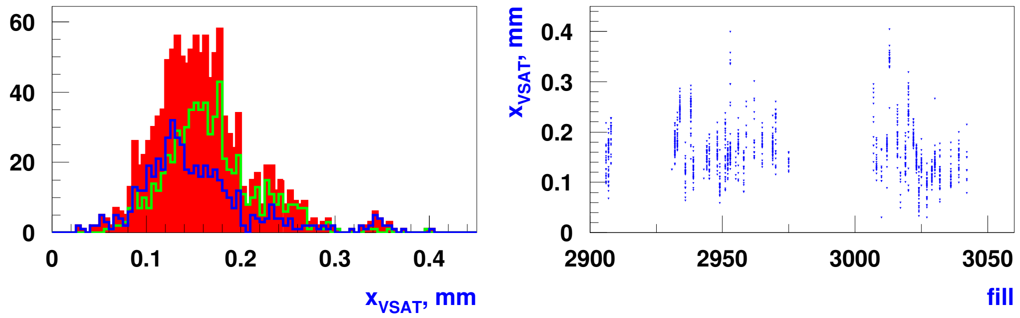

Figure 5.13: *x_{VSAT} with corrections for the beam width, divergence and y-tilt. The x-acollinearity effect has not been included. The green (blue) curve corresponds to data before (after) the accident.*

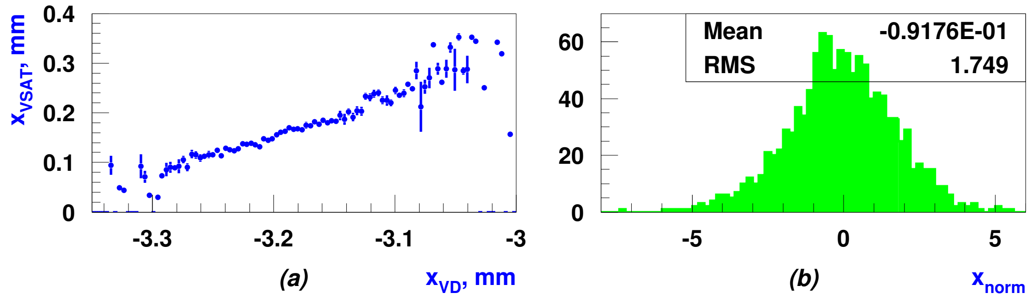

Figure 5.14: *(a) x_{VSAT} from VSAT plotted versus x_{VD}, (b) normalized difference between x_{VSAT} from VSAT and x_{VD}.*

have a significant contribution to the determination of the interaction point. From FASTSIM simulations done for different beam tilts, we estimate that an average fluctuation in acollinearity of the order of 15 μrad is sufficient to produce an additional variation of about 40 μm in the VSAT determination of x_{VSAT} [28]. This could allow us to assume a systematic difference in acollinearity of about 5 μrad in order to explain the shift of the mean value between the periods before and after the accident.

5.3.2 Estimation of the y beamspot

As was mentioned in section 5.2.2, the situation in the (y,z) plane is similar to that in the (x,z) plane, apart from the fact that the effect of the superconducting quadrupoles is here convergent. The reduced sensitivity of the detector thus induced prohibits an estimation of the y beamspot from eq. (5.21). To confirm this, we plot in fig. 5.15 y_{VSAT} from eq. (5.21) versus the y beamspot measurement of the VD. We see that there is no correlation.

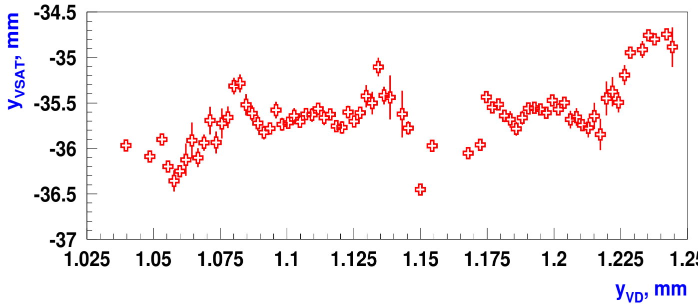

Figure 5.15: *y_{VSAT} versus y_{VD}. ϵ_y was neglected in the VSAT measurement.*

5.3.3 Estimation of the z beamspot

According to the corrections of section 5.3.1, eq. (5.10) gives

$$z_{VSAT} = \frac{\delta x_C}{2 f_x (\theta_1^x + \theta_2^x)} \tag{5.27}$$

where we have substituted z_{VSAT} for z_b for clarity. The sum of the production angles can be derived from the expressions of the impact points, eq. (5.6), as follows:

$$\theta_1^x + \theta_2^x = \frac{x_{F1} - x_{B2} - x_{F2} + x_{B1}}{2 \cdot l_x} \tag{5.28}$$

The estimation of z_{VSAT} is given in fig. 5.16. The mean value before and after the accident was (-45.976 ± 3.316) mm and (-50.195 ± 4.611) mm, respectively. The overall mean value was (-47.769 ± 4.440) mm.

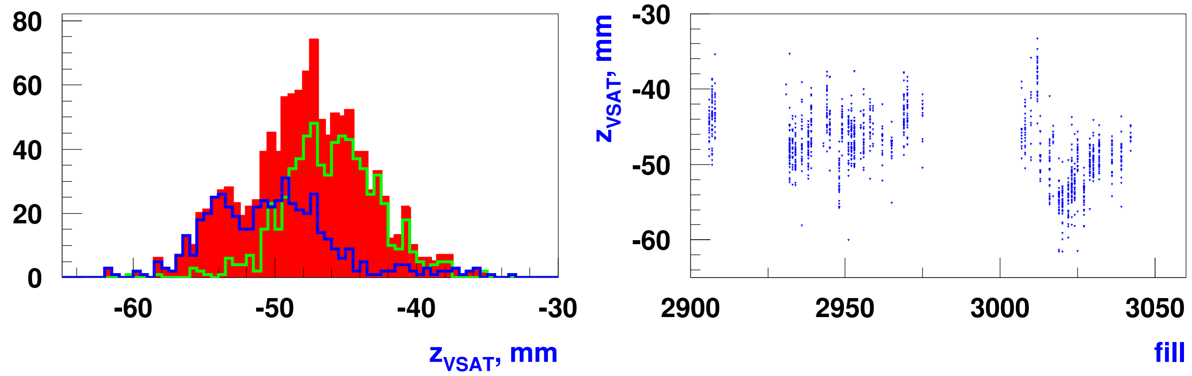

Figure 5.16: *z_{VSAT} with corrections for the beam width, divergence and y-tilt. The x-acollinearity effect has not been included. The green (blue) curve corresponds to data before (after) the accident.*

In fig. 5.17(a), we have plotted the VSAT versus the TPC measurement for the z beamspot. We discern a linear relation as in the case of x_{VSAT} (fig. 5.14(a)). The offset between the two measurements is 35 mm approximately. The normalized difference distribution is given in fig. 5.17(b).

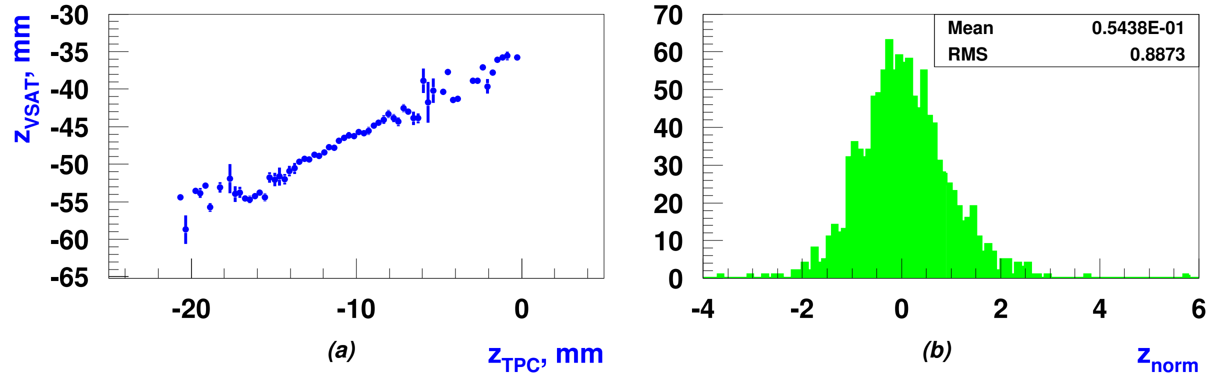

Figure 5.17: *(a) z_{VSAT} versus z_{TPC}, (b) normalized difference between z_{VSAT} and z_{TPC}.*

The rms of fig. 5.17(b) is close to unity as expected. This is because the effect of the acollinearity cancels out in the difference $\Delta x_2 - \Delta x_1$.

5.4 Variation of the asymmetry, tilt and acollinearity.

We can calculate the asymmetry directly from the data by using eq. (5.11), where N_1 and N_2 are the Bhabha events on diagonals 1 and 2, respectively. As was mentioned in section 5.2.1, FASTSIM has provided us with a relation between the asymmetry and the mean tilt angle in the (x,z) plane, which allows us to monitor variations of θ_x according to

$$\theta_x = 1.75 \cdot A_D \tag{5.29}$$

where θ_x is in mrad. It is possible to estimate the mean tilt, θ_y, in the (y,z) plane from the relations giving the y coordinates of the impact points (eq. (5.19)):

$$y_{F1} + y_{F2} - y_{B1} - y_{B2} =$$

$$= 2f_y z_b(\theta_+^y - \theta_-^y) + 2l_y(\theta_1^y - \theta_2^y + \theta_-^y + \theta_+^y) =$$

$$= -2f_y z_b \epsilon_y + 2l_y(\theta_1^y - \theta_2^y) + 4l_y\theta_y \approx$$

$$\approx 4l_y\theta_y$$

and thus

$$\theta_y \approx (y_{F1} + y_{F2} - y_{B1} - y_{B2})/4l_y \tag{5.30}$$

We plot the variation of the asymmetry in fig. 5.18. Its mean value was -0.047 ± 0.022. There is no significant shift before and after the accident. The variation of the mean tilts in the (x,z) and (y,z) planes

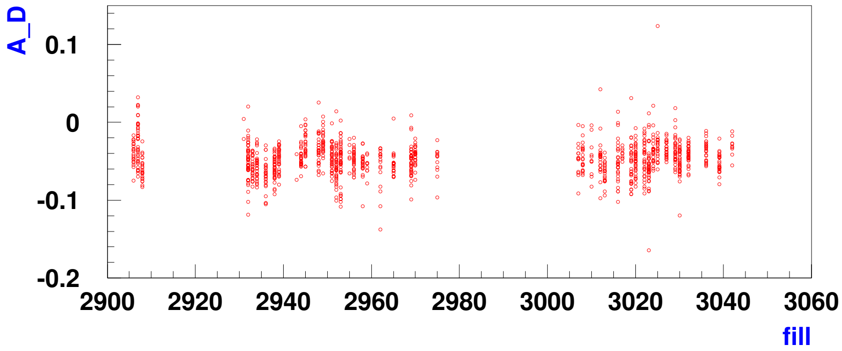

Figure 5.18: *Variation of the asymmetry.*

is given in fig. 5.19. Their mean values were (-0.082 ± 0.038) *mrad* and (0.462 ± 0.076) *mrad*, respectively. The mean values of θ_y before and after the accident were (0.474 ± 0.076) *mrad* and (0.447 ± 0.072) *mrad*, respectively.

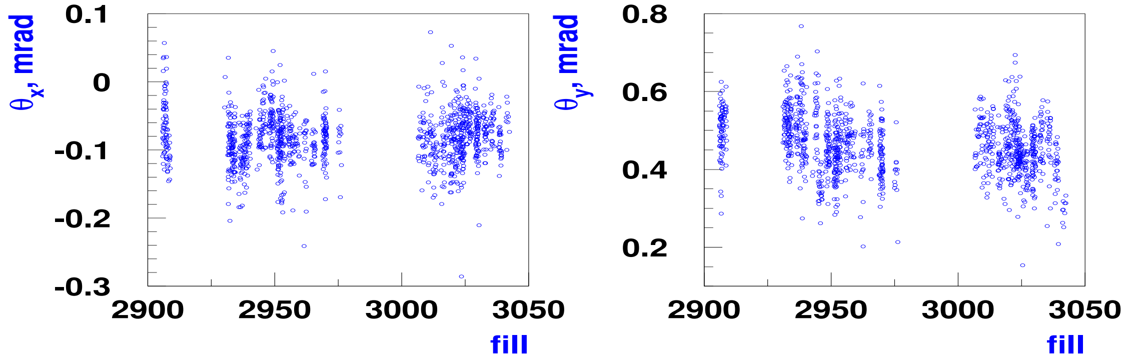

Figure 5.19: *Variations of θ_x and θ_y.*

The VD beamspot data can be used to provide us with information on the acollinearity in (x,z) and (y,z) plane. To this end, we introduce the VD values for x beamspot and y beamspot in eqs. (5.9) and (5.21), from which we obtain the following expressions:

$$\epsilon_x \approx \frac{\Delta x_C - 2f_x \cdot x_{VD}}{l_x} \tag{5.31}$$

$$\epsilon_y \approx \frac{\Delta y - 2f_y \cdot y_{VD}}{l_y} \tag{5.32}$$

We plot the ϵ_x and ϵ_y variations in fig. 5.20. The overall, before and after the accident mean values of

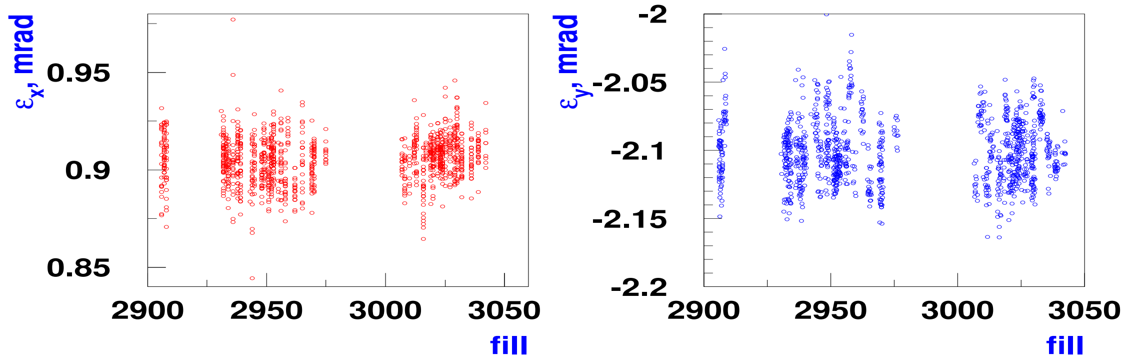

Figure 5.20: *Variation of ϵ_x and ϵ_y*

ϵ_x were (0.905 ± 0.012) *mrad*, (0.904 ± 0.012) *mrad* and (0.907 ± 0.010) *mrad*, respectively. We observe a difference of 3 μrad between the last two values, which agrees with our prediction of 5 μrad in section 5.3.1. The overall mean value of ϵ_y was (-2.101 ± 0.023) *mrad* and it has not showed a shift before and after the accident.

We have mentioned that the effect of the beam widths and divergences on the x_{VSAT} values is detected in terms of $R\Delta x$. We show the variations of this parameter in fig. 5.21. Its overall mean value was (1.937 ± 0.081) *mm*. It mean value before the accident was (1.947 ± 0.080) *mm* and after the accident (1.922 ± 0.080) *mm*.

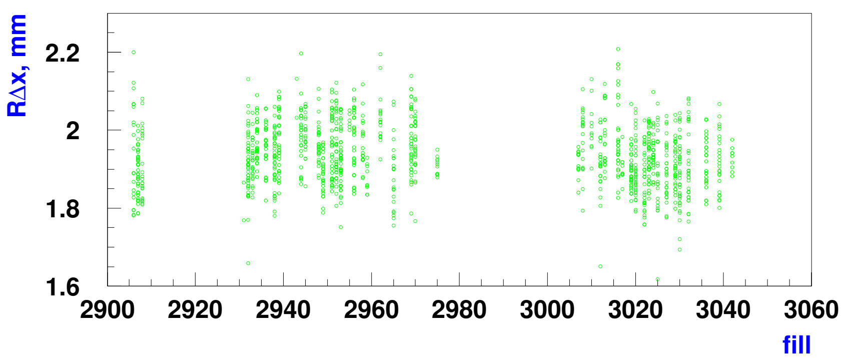

Figure 5.21: *Variation of $R\Delta x$.*

5.5 Dependence on minibunch number.

The only point which is left for us to examine at this stage is whether the beam parameters above depend on the minibunch number. Since all our calculations are based on the x and y values of the particle impact points on the four modules, we plot these values for the three minibunches in figs. 5.21 and 5.22. We observe that there is no dependence on minibunch number.

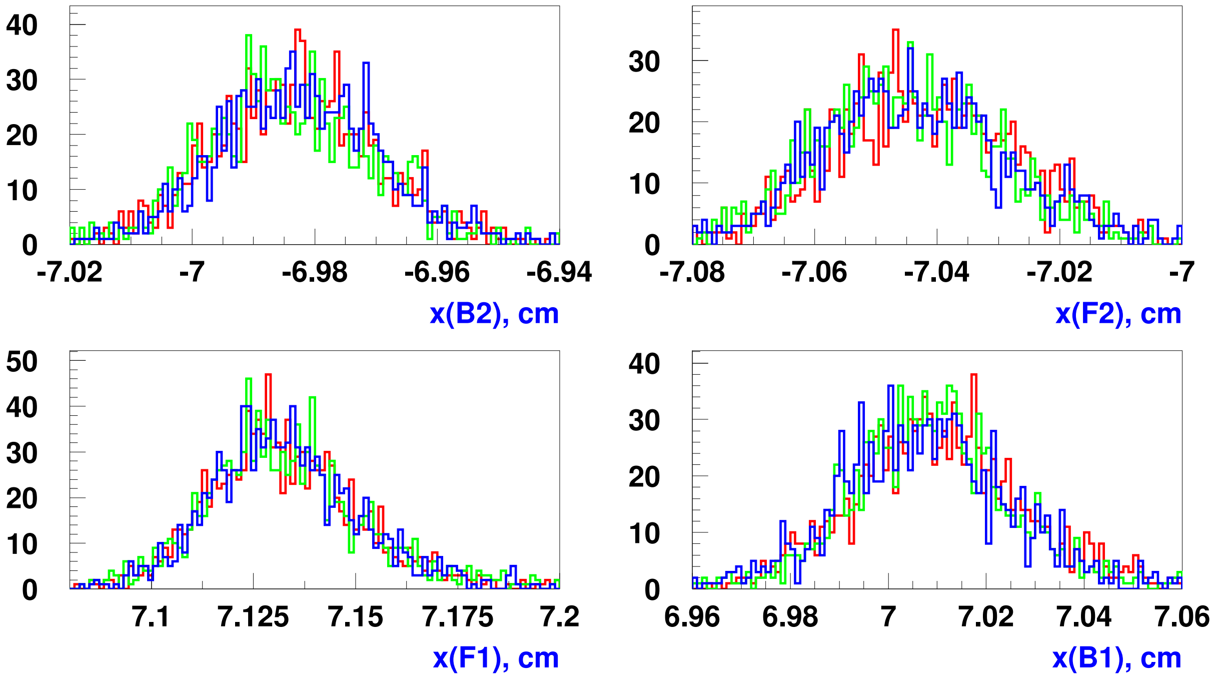

Figure 5.22: *x impact point values for the four modules and minibunch number one (red curves), two (green curves) and three (blue curves).*

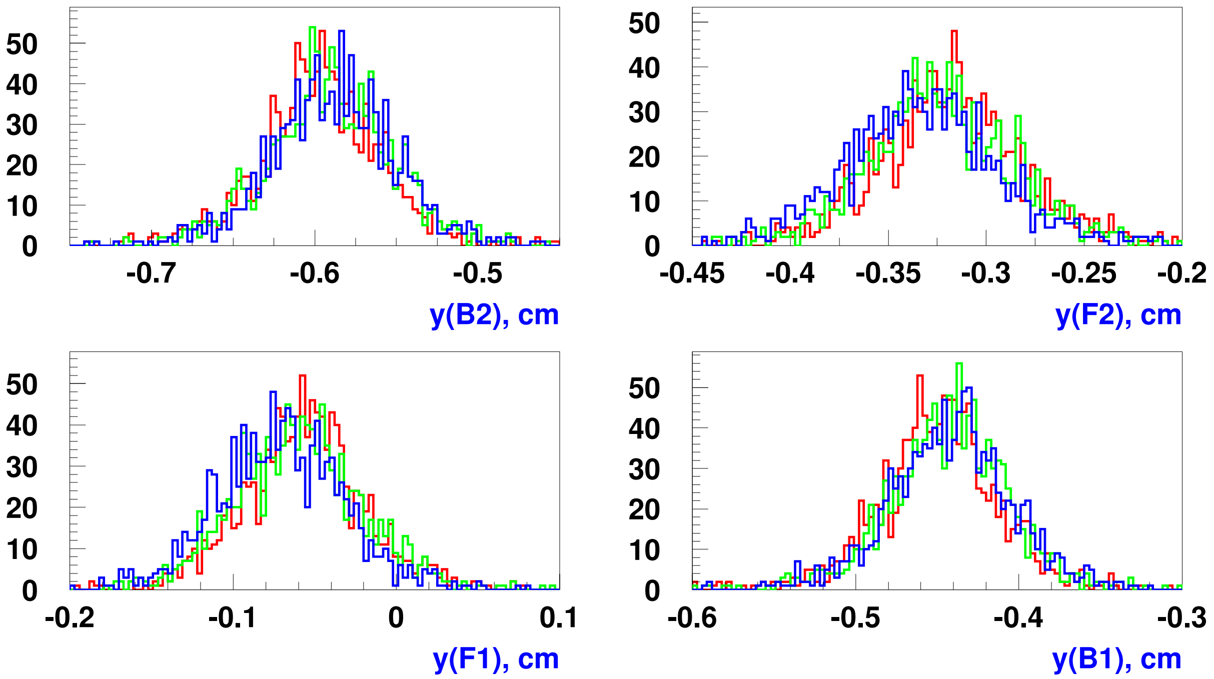

Figure 5.23: *y impact point values for the four modules and minibunch number one (red curves), two (green curves) and three (blue curves).*

Chapter 6

The Simulation

In chapter 4, we described how we obtain the Bhabha sample that we need for the luminosity evaluation. What we need to calculate now is the accepted Bhabha cross section of our detector. This can be determined by convoluting the theoretical cross section with the geometrical acceptance of the VSAT. The analytical calculation is very complicated [9] and the natural way out is to use a simulation instead. We describe this simulation, called FASTSIM, in section 6.1. After calculating the accepted cross section, we have to correct it for the variation of the beam parameters. This is described in section 6.2.

6.1 Description of FASTSIM

6.1.1 Tracking of particles from the interaction point to the VSAT modules

The events are generated with the BHLUMI program [29], where exponentiated corrections (from third order and thereafter) have been implemented giving a theoretical uncertainty of about 0.1%. FASTSIM then tracks the particles from the interaction point to the detector as follows [9].

The path of the scattered particle is divided into three different transport regions. From the interaction point to 3.7 m along the z-direction it passes through the magnetic field of the DELPHI solenoid. After that it travels through the field of the superconducting quadrupoles, which are located between 3.7 m and 5.7 m along the beam axis. The last part of the particle's path is the field-free region between the quadrupoles and the modules, which are placed at 7.7 m from the interaction point.

A convenient way to describe this motion is to use the phase space coordinates x, y, $x' = dx/ds$ and $y' = dy/ds$, where s is the coordinate along the trajectory. The motion of the particle through each of the above mentioned regions can then be represented by a matrix describing the transformation of the phase space coordinates. The path of the particle from the interaction point (ip) to the VSAT module is thus written as:

$$\begin{pmatrix} x \\ x' \\ y \\ y' \end{pmatrix}_{VSAT} = T_3 T_2 T_1 \begin{pmatrix} x \\ x' \\ y \\ y' \end{pmatrix}_{ip} \tag{6.1}$$

where T_1, T_2, T_3 are the transformation matrices for the three transport regions described above.

The transformation of the phase space under the influence of the DELPHI solenoid field can be written by introducing the bending strength of the solenoid field

$$\frac{1}{\rho} = \frac{-0.2998B}{p} \tag{6.2}$$

where B is the magnetic field in Tesla, ρ is the bending radius and p is the particle's momentum in GeV and the corresponding bending angle

$$\phi = \frac{q(z_1 - z_0)}{\rho} \tag{6.3}$$

where q is the charge of the particle and $z_1 - z_0$ is the distance traversed in the magnetic field. The expression for the T_1 matrix is then

$$T_1 = \begin{pmatrix} 1 & q\rho sin\phi & 0 & q\rho(cos\phi - 1) \\ 0 & cos\phi & 0 & -sin\phi \\ 0 & -q\rho(cos\phi - 1) & 1 & q\rho sin\phi \\ 0 & sin\phi & 0 & cos\phi \end{pmatrix} \tag{6.4}$$

The T_2 matrix giving the transformation of the phase space through the quadrupole field is of the form

$$T_2 = \begin{pmatrix} a_{11} & a_{12} & a_{13}(\theta) & a_{14}(\theta) \\ a_{21} & a_{22} & a_{23}(\theta) & a_{24}(\theta) \\ a_{31}(\theta) & a_{32}(\theta) & a_{33} & a_{34} \\ a_{41}(\theta) & a_{42}(\theta) & a_{43} & a_{44} \end{pmatrix} \tag{6.5}$$

The T_2 matrix elements are functions of the length and strength of the quadrupole field and also of the momentum of the particle. For a quadrupole field the focusing or defocusing effect in one direction (x or y) depends only on the phase space components in that direction (i.e. x and y are decoupled). However, the quadrupoles are rotated by an angle θ with respect to the VSAT coordinate system. Therefore, the coordinates of the particle have to be rotated into the quadrupole coordinate system before making the transformation through the quadrupoles and rotated back afterwards. Consequently, the elements in the upper right and lower left part of the matrix, connecting the vertical and horizontal coordinates, will be dependent on the rotation angle θ.

The region between 5.7 m and 7.7 m being a field-free region, the matrix T_3 is simply

$$T_3 = \begin{pmatrix} 1 & z_3 - z_2 & 0 & 0 \\ 0 & 1 & 0 & 0 \\ 0 & 0 & 1 & z_3 - z_2 \\ 0 & 0 & 0 & 1 \end{pmatrix} \tag{6.6}$$

where z_3 is the z position of the VSAT module and z_2 is the exit of the quadrupole.

With the values of T_1, T_2 and T_3 inserted into eq. (6.1), a relation between the phase space of the electron at the interaction point and at the impact point on VSAT module 1 is derived, e.g.

$$x_{v1} = A_{x1}x'_{ip} + B_{x1}x_{ip} + (C_x + D_x)y'_{ip} + E_x y_{ip} \tag{6.7}$$

The effect of the solenoid field is contained in the constant D_x and the effect of the relative orientation between LEP and DELPHI horizontal planes is manifested in the constants C_x and E_x.

Since a Bhabha event is defined as a coincidence between two diagonal modules, we also need to track the positron to the opposite module (index 2) from the interaction point. Under the assumption of collinear Bhabha events the slopes x' and y' are equal for the two particles and the relation for the positron reads

$$x_{v2} = A_{x2}x'_{ip} - B_{x2}x_{ip} + (C_x - D_x)y'_{ip} - E_x y_{ip} \tag{6.8}$$

The particle on module 2 is on the opposite side in x and y with respect to the first module, which gives the minus sign in front of the second term above. The contribution to the bending of the trajectory in x from the solenoidal field is in the same direction for the electron and the positron, giving the minus sign in front of the constant D_x, while the part belonging to the rotation (constant E_x) between LEP and DELPHI coordinate systems affects the particle trajectories in opposite directions.

The constants A to E in the two equations above, together with the corresponding set of constants for the transformation of the remaining phase space components, define the acceptance in phase space for a pair of diagonal VSAT modules.

The particles that hit the flanges or the material in front of them are discarded in the simulation. Behind the flanges the beam pipe is made of 1.5 mm of aluminium, which corresponds to 0.017 r.l., so it is possible that their shower starts when they hit the beam pipe. FASTSIM calculates the thickness of the traversed material and adds it on the front of the module. The difference from real life is then that the angle between the shower products at the module's front face is not taken into account but this has no significant effect on the analysis [1]. Particle synchrotron radiation in the magnetic fields is also neglected.

6.1.2 The shower parametrization

Once a particle has hit the detector, FASTSIM will simulate the electromagnetic shower which is produced in the module. Both the longitudinal and transverse shower profiles are parametrized to avoid time consuming shower evolutions.

The longitudinal profile parametrization we use is the one determined in [31], where a study was made for a Si/W sandwich calorimeter which contained 24 radiation lengths of tungsten. A silicon detector with 25 cm^2 of active area was located after every two radiation lengths. The energies of the incoming electrons were between 4 and 49 GeV. Only electrons entering the central 0.25 cm^2 region were selected.

The data were fitted by the function

$$\epsilon(t) = \epsilon_0 (t/2)^a exp(-bt) + \epsilon_1 (t/2)^c exp[-m(t - x_1) - y_1] \tag{6.9}$$

where $\epsilon(t)$ is the detected energy in MeV at depth t, expressed in radiation lengths, ϵ_0 and ϵ_1 are normalization constants in MeV, a, b, c, m, x_1 are dimensionless functions of the incident electron energy and y_1 is a dimensionless constant:

$$a = (3.2 \pm 0.5) + (0.3 \pm 0.2) lnE,$$

$$b = (0.75 \pm 0.10) + (-0.05 \pm 0.04) lnE,$$

$$c = (0.26 \pm 0.10) lnE,$$

$$m = (0.04 \pm 0.02) lnE,$$

$$x_1 = (-6.8 \pm 3.5) + (55.9 \pm 20.3) lnE,$$

$$y_1 = 2.5 \pm 0.4,$$

$$\epsilon_0 = (2.2 \pm 1.2) + (1.5 \pm 0.6) lnE,$$

$$\epsilon_1 = 1\ MeV.$$

The transverse profile parametrization was obtain by fits on VSAT data from the x and y strip planes [32]. The formula reads

$$d(r) = a_1 exp(-r/b_1) + a_2 exp(-r/b_2) \tag{6.10}$$

where $d(r)$ is the detected energy at radius r, expressed in radiation lengths, from the impact point divided by the total energy deposit in the plane, a_1 is a dimensionless function of the depth t in radiation lengths, a_2 is a dimensionless constant and b_1, b_2 are constants in radiation lengths:

$$a_1 = 1.11 exp[-(t - 7)/3.97],$$

$$a_2 = 0.1,$$

$$b_1 = 0.082764\ r.l.,$$

$$b_2 = 0.6168\ r.l..$$

The simulated energy at a certain depth t will then be proportional to the quantity

$$signal(t) = \epsilon(t) \int d(r) dr \tag{6.11}$$

where the integral is calculated over the surface of the FAD plane located at depth t. The sum $\sum_t signal(t)$ over all FADs is proportional to the energy deposited in the module and is the equivalent of the uncalibrated energy of the data.

[1] A detailed description of the beam pipe in FASTSIM can be found in [30].

6.1.3 The accepted cross section

After FASTSIM has calculated the energy and position of the particles that hit the detector, the events are analyzed by the same program we analyze the data with. This program applies the energy and position cuts we described in chapter 4. The result of the program is a sample of accepted Bhabha events like the one represented by the blue points in fig. 4.7. The way we calculate the accepted cross section from these events is the following [32]. BHLUMI generates events according to the Born cross section and then modifies it by adding the radiative corrections. If σ_g is the (differential) Born cross section for a particular event and σ_i is the same cross section with all corrections, a weight $w_i = \sigma_i/\sigma_g$ is assigned to the event. After the event has passed the detector simulation and the experimental cuts we can calculate the average weight for all the accepted events

$$\overline{w} = \frac{\sum_{acc} w_i}{N_{generated}} \tag{6.12}$$

where $N_{generated}$ is the number of generated events. The accepted cross section is then calculated as

$$\sigma_{acc} = \overline{w} \cdot \sigma_{approx}. \tag{6.13}$$

where σ_{approx} is the integrated Born cross section for the kinematical region which was used for the run of BHLUMI.

6.2 Correction of the cross section for beam parameter variations

In order to correct the accepted cross section for the variation of the beam parameters in the 1995 scan, 29 FASTSIM runs were done. In 21 runs the x beamspot and the electron and positron divergences in x were varied. In the remaining 8 runs the electron and positron tilts in y were varied [32]. All runs had 1.2 million generated events, except 9 of the 21 first runs, which had 2 million generated events.

Before correcting the cross section we had to check that the simulation agreed with the data. To this end we compared the distributions of the x and y coordinates of the impact points on the four modules (fig. 6.1). One entry in the plots of fig. 6.1 corresponds to one run of data (i.e. one cassette) or to one run of simulation. One simulation run contains about 40000 accepted Bhabha events, so the FASTSIM distributions are only seemingly of low statistics. The difference in shape between the data and FASTSIM distributions is not a disagreement. It is due to the fact that in our plots we have the mean values of the cassettes and not the distributions of the events themselves. The simulation distributions are flat because we chose to do the same number (one) of runs for each set of beam parameters whereas LEP is running for different time intervals at each such set. Our purpose was to produce simulated spectra which would be at about the same range as the data [32]. The small departures seen have no real influence on the final measurement.

We can now do the correction of our cross section. This is done in terms of variables which are directly measured by the detector as follows [25]. For each FASTSIM run and for each diagonal i we calculate the accepted cross section σ_i and the following variables: $\Delta x_i, R\Delta x_i, \Delta y_i$. We also calculate the asymmetry, A_D. Then the correction for the cross section of diagonal i will be

$$\sigma_i = \sigma_0[1 + a_i(\Delta x_i - \overline{\Delta x_i}) + b_i(\Delta x_i - \overline{\Delta x_i})^2 + c_i(\Delta y_i - \overline{\Delta y_i}) + d_i(R\Delta x_i - \overline{R\Delta x_i}) + e_i(A_D - \overline{A_D})] \tag{6.14}$$

The mean values are those of the entire scan data. σ_0 is treated as an unknown constant. In order to calculate the coefficients (slopes) a_i, b_i, c_i, d_i, e_i we do fits to the corresponding distributions of σ_i. e.g. to calculate c_i we do a linear fit to the distribution of σ_i versus $\Delta y_i - \overline{\Delta y_i}$, etc. The results are given in the Table 6.1 [25]. The small differences between diagonals 1 and 2 are due to small asymmetries in the setup.

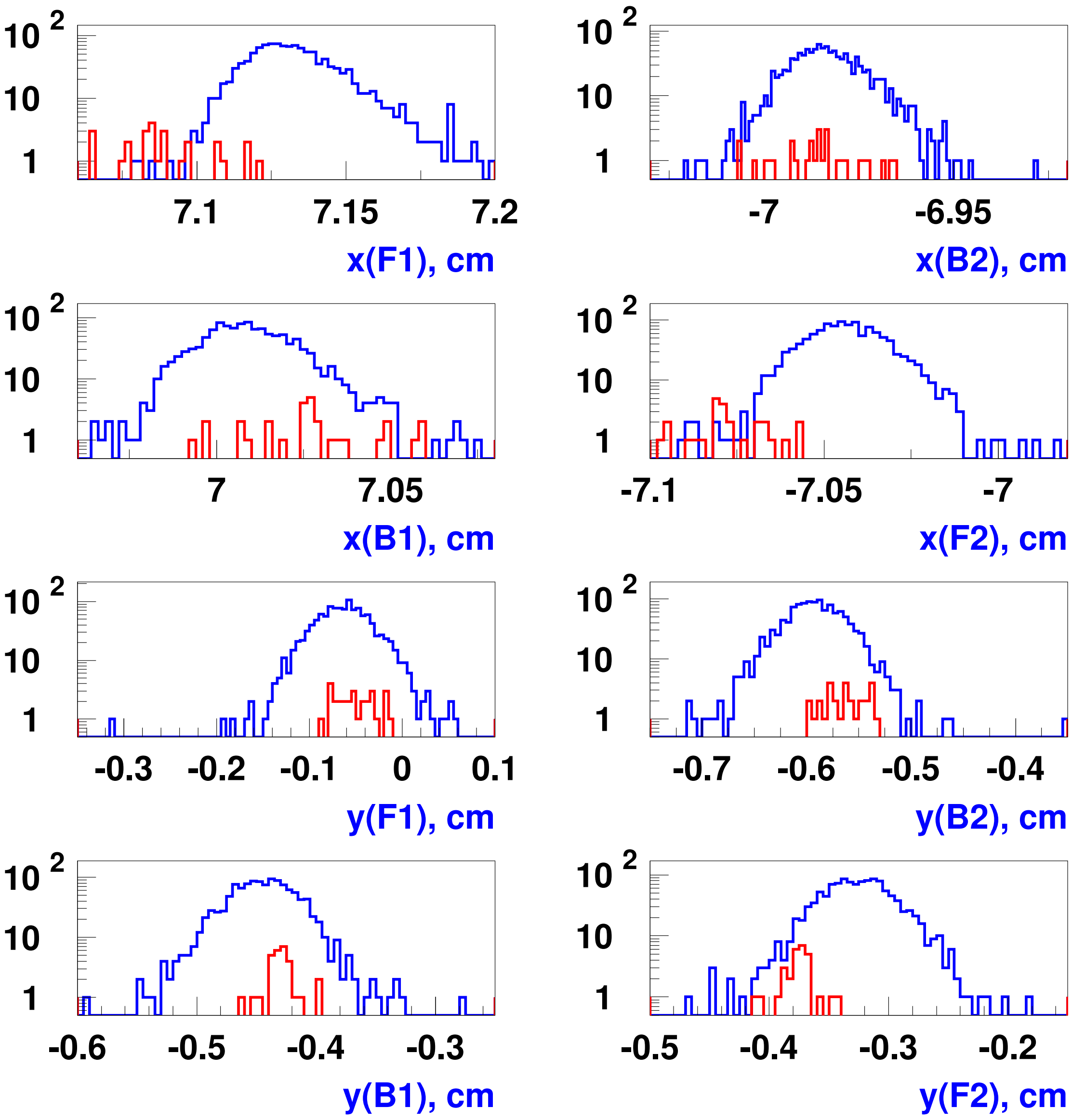

Figure 6.1: *Comparison between data (blue curves) and FASTSIM (red curves) .*

	value for i=1	value for i=2
a_i	0.400 $\pm$ 0.030	-0.128 $\pm$ 0.020
b_i	1.800 $\pm$ 0.700	0.200 $\pm$ 0.500
c_i	-0.090 $\pm$ 0.030	-0.190 $\pm$ 0.030
d_i	0.300 $\pm$ 0.100	0.300 $\pm$ 0.100
e_i	0.001 $\pm$ 0.040	0.001 $\pm$ 0.040

Table 6.1: *Slopes for the 1995 scan .*

Chapter 7

Results

7.1 Relative luminosity

According to eq. (6.14), the number of accepted Bhabha events in the data has to be corrected as follows

$$N^j = \frac{N_1^j}{1 + a_1(\Delta x_1^j - \overline{\Delta x_1^j}) + \ldots} + \frac{N_2^j}{1 + a_2(\Delta x_2^j - \overline{\Delta x_2^j}) + \ldots} \tag{7.1}$$

where N^j is the corrected number of events for the j-th cassette, N_i^j is the number of accepted Bhabha events in diagonal i and the denominators contain all the beam parameter corrections that we discussed in the previous chapter. We calculate the VSAT relative luminosity by adjusting the value of σ_0 so that the normalized differences with the STIC luminosity will be close to zero for the total data sample. The results are given in Table 7.1. The first four lines give the VSAT luminosity. Its values for all minibunch numbers, for minibunch one, two and three are given in lines one, two, three and four, respectively. The next four lines give the corresponding values for STIC luminosity. Then the corresponding numbers of VSAT and STIC Bhabha events are mentioned. In the last line of the table, we give the normalized differences (pulls) between VSAT and STIC luminosities for all minubunch numbers. We see that the pulls are acceptable. The values of the third, four and fifth column represent data taken at 45.66 GeV (peak), 44.74 GeV (peak-2) and 46.51 GeV (peak+2), respectively. The quantities in the last column refer to all energies.

In Table 7.2 we give the errors for the VSAT luminosity. The total error is calculated by adding quadratically the statistical error and the systematic error. The systematic error stems from the cross section correction for the beam parameters. For example, the correction for $R\Delta x_1$ is $d_1(R\Delta x_1 - \overline{R\Delta x_1})$, where d_1 is the slope, i.e. the correction factor given by FASTSIM, $R\Delta x_1$ is the value of $R\Delta x_1$ of the cassette currently processed and $\overline{R\Delta x_1}$ is the average value of $R\Delta x_1$ over all scan data. As a consequence, there are two contributions to the error, one due to the error of the slope, which comes from FASTSIM and is called correlated systematic error and the other being the error of $R\Delta x_1$ (depending on the statistics of the cassette) called uncorrelated systematic error. We also state the STIC error for comparison. The total VSAT error is significantly better than the STIC error.

7.2 Z^0 lineshape

In Appendix A we give the DELPHI results on the hadronic cross sections and the cross sections and forward-backward asymmetries in the leptonic channels for the data taken from 1993 to 1995 at the Z^0 peak. The contribution of our analysis, i.e. the measurement of the relative luminosity for the 1995 scan, was to cross check the stability of the STIC luminosity. The STIC and VSAT measurements were not combined, as was done in 1993, for two reasons. First, the statistical STIC error was better than the error of the calorimeter it has replaced (SAT). Second, the VSAT lost a considerable amount of data taken at peak, which shows in the much larger corresponding pull when comparing with 1993 data.

	mb	peak	peak-2	peak+2	total
L^{int}_{VSAT} (nb^{-1})		1752.54	4619.77	5520.35	11892.64
	1	580.63	1628.97	1951.87	4161.47
	2	619.18	1549.52	1870.15	4038.85
	3	550.50	1434.84	1691.23	3676.57
L^{int}_{STIC} (nb^{-1})		1736.78	4640.97	5515.72	11893.46
	1	571.33	1628.97	1948.72	4149.02
	2	614.71	1565.19	1873.14	4053.04
	3	550.21	1445.61	1692.03	3687.85
$Bhabhas_{VSAT}$		612277	1681154	1859281	4152713
	1	202853	592796	657399	1453049
	2	216321	563872	629871	1410065
	3	192327	522148	569616	1284091
$Bhabhas_{STIC}$		95232	266399	290134	651765
	1	31331	93499	102504	227334
	2	33705	89852	98533	222090
	3	30166	82978	89001	202145
Pull		2.47	-2.63	-0.01	-0.66

Table 7.1: *STIC and VSAT luminosities.*

	mb	peak	peak-2	peak+2	total
STATISTICAL (permille)		1.28	0.77	0.73	0.49
	1	2.22	1.30	1.23	0.83
	2	2.15	1.33	1.26	0.84
	3	2.28	1.38	1.33	0.88
UNC. SYSTEMATIC (permille)		0.28	0.17	0.16	0.11
	1	0.50	0.29	0.28	0.18
	2	0.48	0.29	0.28	0.19
	3	0.51	0.31	0.30	0.20
COR. SYSTEMATIC (permille)		0.34	0.42	0.37	0.09
	1	0.41	0.52	0.26	0.22
	2	0.33	0.41	0.49	0.19
	3	0.36	0.43	0.47	0.11
TOT. SYSTEMATIC (permille)		0.44	0.45	0.41	0.14
	1	0.64	0.59	0.38	0.29
	2	0.58	0.50	0.56	0.26
	3	0.62	0.53	0.56	0.22
TOTAL ERROR (permille)		1.35	0.89	0.84	0.51
	1	2.31	1.43	1.29	0.88
	2	2.23	1.42	1.38	0.88
	3	2.36	1.48	1.44	0.91
$error_{STIC}$ (permille)		3.24	1.94	1.85	1.24
	1	5.64	3.27	3.12	2.10
	2	5.44	3.33	3.18	2.12
	3	5.75	3.47	3.35	2.22

Table 7.2: *STIC and VSAT errors.*

Acknowledgements

There are many people I would like to thank because without their help this report would not have been written. I will mention here only a few.

First of all, I would like to thank my supervisors, Giuseppina Rinaudo and Bengt Lörstad, for their guidance, help and support during all the time I have been working with the VSAT. I would also like to thank Gösta Gustafson and Torbjörn Sjöstrand for their patience with my questions about Bhabha scattering and for their help with the coursework. For this latter reason I would also like to thank Anders Irbäck, Erik Sandelin and Henrik Jönsson.

Many thanks are also due to Mikael Eriksson for his help with accelerator physics, to Philippe Charpentier for information on online luminosity, to Vincent Hedberg for information on the STIC and help with data analysis and to Michele Caffo for restoring the program bhabha.for and discussing the corrections with me. I would also like to thank Helmut Burkhardt for allowing me to use figure 2.2. I owe my gratitude to the people that have worked with the VSAT, Per Jonsson, Nikolai Zimin, Henrik Carling, Ulf Mjörnmark, Fabio Cossutti, Andreas Nygren and Björn Lundberg for their collaboration and friendship. Sverker Almehed deserves a special mention for answering endless questions about the simulation and the analysis in general. I would also like to thank Jean-Paul Chavanel for his help with our vax disks.

Lastly, I would like to thank Oxana Smirnova for being a great friend and helping practically with everything. I owe my deepest gratitude to my parents for their unfailing help and support, without which this work would not have been possible.

Bibliography

[1] S. Myers, *The LEP collider*, excerpts from The John Adams Memorial Lecture, CERN, 26 November 1990.

[2] T. Camporesi et al., *Luminosity Measurement in 1994 with the STIC detector*, DELPHI 97-08 PHYS 667.

[3] M. Paganoni et al., *Energy and position reconstruction in the DELPHI Small Angle Tile Calorimeter*, DELPHI 97-07 PHYS 666.

[4] E. Falk et al., *Simulation of Off-Energy Electron Background in DELPHI*, DELPHI 97-12 LEDI 8.

[5] E. Falk et al., *Photon Analysis with STIC*, DELPHI note in preparation.

[6] Ch. Jarlskog, *Interaction point estimation and beam parameter variations in DELPHI with the VSAT*, LUNFD6/(NFFL-7110)1995.

[7] K. Potter, *Luminosity measurements and calculations*, CERN Accelerator School 1992, CERN 94-01.

[8] H. Wiedemann, *Particle Accelerator Physics*, Springer-Verlag 1993, chapter 12.

[9] A. Håkansson, *Luminosity Measurement at LEP using the Very Small Angle Tagger of DELPHI*, PhD thesis, LUNFD6/(NFFL-7077) 1993.

[10] F. M. Renard, *Basics of Electron Positron Collisions*, éditions Frontières, 1981.

[11] D. H. Perkins, *Introduction to High Energy Physics*, Addison-Wesley, 1987, chapter 2.

[12] H. Wiedemann, *Particle Accelerator Physics*, Springer-Verlag 1993, chapter 7.

[13] P. M. Jonsson, *Luminosity Measurements and Two-Photon Physics with the DELPHI VSAT at LEP*, PhD thesis, LUNFD6/(NFFL-7152) 1998.

[14] S. J. Alvsvaag at al., *The system for online monitoring of LEP beam background and luminosity at the DELPHI interaction point*, DELPHI 93-3 DAS 137.

[15] *Bhabha Scattering* in *Z Physics at LEP 1*, volume 1, CERN 98-08, convenors M. Caffo and E. Remiddi.

[16] M. Caffo, private communication.

[17] *Electroweak radiative corrections for Z physics* in *Z Physics at LEP 1*, volume 1, CERN 98-08, convenors M. Consoli and W. Hollik.

[18] M. Greco, *Bhabha scattering near the Z^0*, Physics Letters B **177** (1986) 97-105.

[19] M. Caffo et al., *Hard collinear photons, high-energy radiative corrections to Bhabha scattering*, Nuclear Physics **B252** (1985) 378-388.

[20] M. Böhm et al., *Radiative corrections to Bhabha scattering at high energies (I)*, Nuclear Physics **B304** (1988) 687-711.

[21] U. Mjörnmark, private communication.

[22] Ch. Jarlskog, *VSAT Off-line Minibunch Tagging for the 1995 Scan*, LUNFD6/(NFFL-7154) 1998, internal report in preparation.

[23] Ch. Jarlskog, *VSAT energy calibration for 1995 minibunch data*, LUNFD6/(NFFL-7129) 1996.

[24] I. Kronkvist, *Data Base and Slow Controls System of the DELPHI VSAT and Two-Photon Physics using DELPHI at LEP* , PhD thesis, LUNFD6/(NFFL-7128) 1996.

[25] G. Rinaudo, private communication.

[26] S. Almehed at al., *Measurement of the beam parameter variations in DELPHI with the VSAT*, DELPHI 95-150 LEDI 2.

[27] Ch. Jarlskog, *Beam Parameter Analysis for the VSAT* , LUNFD6/(NFFL-7145) 1997.

[28] S. Almehed et al., *High precision relative luminosity measurement with a Very Small Angle Tagger (VSAT) in DELPHI*, DELPHI 92-77 PHYS 188.

[29] S. Jadach et al., *Multiphoton Monte Carlo event generator for Bhabha scattering at small angles*, Phys. Rev. D, **40**, 3582, 1989.

[30] I. Kronkvist, *FASTSIM examination on how different LEP beam parameters affect the acceptance of the VSAT detector* , LUNFD6/(NFFL-7061) 1990.

[31] G. Barbiellini et al., *Energy resolution and longitudinal shower development in a Si/W electromagnetic calorimeter* , NIM A235 (1985) 55-60.

[32] S. Almehed, private communication.

List of Figures

Appendix A

Cross Sections and Leptonic Forward-Backward Asymmetries from the Z^0 Running of LEP